

Combining analytic preconditioner and Fast Multipole Method for the 3-D Helmholtz equation[☆]



M. Darbas^a, E. Darrigrand^{b,*}, Y. Lafranche^b

^a LAMFA UMR CNRS 7352, Université de Picardie, Amiens, France

^b IRMAR UMR CNRS 6625, Université de Rennes 1, Rennes, France

ARTICLE INFO

Article history:

Received 16 April 2012

Received in revised form 26 October 2012

Accepted 27 October 2012

Available online 28 November 2012

Keywords:

Integral equation methods

Analytic preconditioner

FMM

High-frequency scattering

Helmholtz

ABSTRACT

The paper presents a detailed numerical study of an iterative solution to 3-D sound-hard acoustic scattering problems at high frequency considering the Combined Field Integral Equation (CFIE). We propose a combination of an OSRC preconditioning technique and a Fast Multipole Method which leads to a fast and efficient algorithm independently of both a frequency increase and a mesh refinement. The OSRC-preconditioned CFIE exhibits very interesting spectral properties even for trapping domains. Moreover, this analytic preconditioner shows highly-desirable advantages: sparse structure, ease of implementation and low additional computational cost. We first investigate the numerical behavior of the eigenvalues of the related integral operators, CFIE and OSRC-preconditioned CFIE, in order to illustrate the influence of the proposed preconditioner. We then apply the resolution algorithm to various and significant test-cases using a GMRES solver. The OSRC-preconditioning technique is combined to a Fast Multipole Method in order to deal with high-frequency 3-D cases. This variety of tests validates the effectiveness of the method and fully justifies the interest of such a combination.

© 2012 Elsevier Inc. All rights reserved.

1. Introduction

In this paper, we consider the problem of high-frequency scattering of time-harmonic acoustic waves by a bounded sound-hard obstacle in three dimensions. Integral equation methods are used extensively for numerical computations of solutions to such homogeneous scattering problems. These approaches apply the Green's function formalism to reduce the dimensionality of the problem by one. The governing boundary-value problem is then reduced to an integral equation on the surface of the scatterer. The integral operators involved in these formulations are nonlocal and the discretization gives rise to dense matrices. Moreover, one has to consider a sufficient number of points per wavelength (about 10 points) to capture the oscillatory behavior of the wave at high frequencies. The solution of these large and dense linear systems are handled by Krylov-subspaces iterative solvers (e.g. GMRES [47]). The number of iterations to reach the convergence is strongly linked to the spectral properties of the underlying integral operators. To be able to predict the convergence, one therefore needs to investigate the eigenvalue distribution of the integral formulations for acoustic scattering problems. We focus on the class of Combined Field Integral Equations (CFIE) [12,15,23,40] that share the unique solvability property in appropriate functional spaces. Recent studies have been achieved to understand the dependence of the condition number of

[☆] This work was funded in part by the project ANR MicroWave.

* Corresponding author.

E-mail addresses: marion.darbas@u-picardie.fr (M. Darbas), eric.darrigrand-lacarrière@univ-rennes1.fr (E. Darrigrand), yvon.lafranche@univ-rennes1.fr (Y. Lafranche).

the CFIE formulations in terms of both frequency and mesh size [10,11,25]. For a sound-hard obstacle, the CFIE formulations involve the boundary Neumann trace of the double-layer potential which is a pseudodifferential operator of order 1 [48]. Thus, these formulations are integral equations of the first-kind and a sequence of corresponding eigenvalues tends to infinity. The condition number of the CFIE formulations grows not only with the mesh discretization density but also with the frequency. Thus, to make possible the use of iterative solvers for scattering problems, two kind of techniques have been investigated for years: fast methods for the computation of matrix–vector products and preconditioners to speed up the convergence of the solver.

On the one hand, for the numerical resolution of integral equations, it is still of importance to use a fast method for the consideration of the integral operators of the initial equation. The Fast Multipole Method (FMM) is such a method that speeds up the calculation of matrix–vector products where the matrix is obtained by discretization of an integral operator. The method has been introduced by Rokhlin and co-workers (e.g. [22]) and was adapted to integral equations of wave propagation in the 90s (e.g. [20,28,29,35,45]). The discretization of integral operators leads to dense matrices which correspond to interactions between the degrees of freedom. The FMM strategy is essentially based on a choice of an expansion of the Green's kernel and a distribution of the degrees of freedom into boxes such that the interactions between the degrees of freedom are replaced by interactions between boxes. For Helmholtz fundamental solution, the most popular expansion is given from the Gegenbauer series and the Funk–Hecke formula. It leads to a robust method at high frequency but that suffers from instabilities in the low-frequency regimes. However, strategies have been under development for a new expansion available at any frequency regime (e.g. [30,39]).

On the other hand, efficient preconditioners have to be prescribed to yield fast convergence independent of both mesh size and frequency. A first solution is to apply algebraic preconditioning techniques, like SPAI (SParse Approximate Inverse) [16,17] or multi-grids methods [18]. However, even if these preconditioners improve solver performance, slow convergence and convergence breakdown still arise when medium and high frequencies are considered. Analytic preconditioners offer a very interesting alternative. This approach uses pseudo-inverse of the hypersingular operators. A judicious integral representation of the scattered field as a linear combination of single- and regularized double-layer potentials is considered. The objective is to force the boundary integral operator arising from this representation to become a compact perturbation of the identity operator. Several well-conditioned CFIE have been proposed recently [1,6,7,13]. We consider in this paper a pseudo-differential operator preconditioning technique developed by Antoine and Darbas [6,7]. The so-called regularizing operator is a high-frequency approximation to the Neumann-to-Dirichlet operator, and is constructed in the framework of the On-Surface Radiation Conditions method [38,34,4,8]. The implementation of the underlying OSRC-preconditioned CFIE has already been made, which validates the approach [25]. Moreover, we emphasize highly-desirable advantages of this technique:

- the Padé-approximation of the regularizing pseudo-differential operator leads to a sparse matrix involving only the mass and rigidity finite element matrices which makes its implementation rather easy,
- in the framework of an iterative solver, the additional computational cost per iteration is thus negligible compared to the one related to the integral operators,
- to deal with high-frequencies, the resolution requires fast methods such as the FMM. Both techniques, the fast method and the preconditioner, do not interact and are complementary.

This paper is organized as follows. In Section 2, we describe the scattering problem and recall the basic tools to obtain integral equations. In Section 3, we introduce the classical and OSRC-preconditioned CFIEs that we use. In Section 4, we present the discretization and the resolution of the integral equation formulations. In Section 5, we introduce the geometries considered for the numerical tests. Section 6 is devoted to a numerical investigation of the eigenvalues of the classical and OSRC-preconditioned CFIEs operators. Finally, in Section 7, we provide various numerical illustrations of the efficiency of the method in terms of computation cost and speed of convergence. They show the adequacy with the spectral analysis (Section 6) with or without FMM.

2. The Helmholtz exterior problem and integral representation

Let us consider a bounded domain $\Omega^- \subset \mathbb{R}^3$ representing an impenetrable body with Lipschitz continuous boundary $\Gamma := \partial\Omega^-$. We denote by $\Omega^+ := \mathbb{R}^3 \setminus \overline{\Omega^-}$ the associated homogeneous exterior domain of propagation. We are concerned with the scattering of an incident time-harmonic acoustic wave u^{inc} by the obstacle Ω^- . We consider an incident plane wave of the form

$$u^{\text{inc}}(\mathbf{x}) = e^{-ik\xi^{\text{inc}} \cdot \mathbf{x}},$$

characterized by the wavenumber $k := 2\pi/\lambda$, setting λ as the wavelength of the signal. The direction of incidence $-\xi^{\text{inc}}$ is defined by

$$\xi^{\text{inc}} = (\cos(\theta^{\text{inc}}) \sin(\varphi^{\text{inc}}), \sin(\theta^{\text{inc}}) \sin(\varphi^{\text{inc}}), \cos(\varphi^{\text{inc}}))^T.$$

The scattering angles $(\theta^{\text{inc}}, \varphi^{\text{inc}})$ are expressed in the spherical coordinates system. The scattered field u^+ satisfies the Helmholtz exterior boundary-value problem

$$\begin{cases} \Delta u^+ + k^2 u^+ = 0, & \text{in } \Omega^+, \\ \partial_{\mathbf{n}} u^+|_{\Gamma} = g = -\partial_{\mathbf{n}} u^{\text{inc}}|_{\Gamma}, & \text{on } \Gamma, \\ \lim_{|\mathbf{x}| \rightarrow +\infty} |\mathbf{x}| \left(\nabla u^+ \cdot \frac{\mathbf{x}}{|\mathbf{x}|} - iku^+ \right) = 0. \end{cases} \quad (1)$$

We focus on a sound-hard boundary condition on Γ . Vector \mathbf{n} is the unit normal to Γ outwardly directed from Ω^- . The last equation is the Sommerfeld radiation condition which describes the behavior of the solution at infinity. We have the following existence and uniqueness result (see for instance [40]).

Theorem 1. *We assume that*

- Ω^- is a bounded region in \mathbb{R}^3 with Lipschitz continuous boundary Γ ,
- $g \in H^{-1/2}(\Gamma)$.

Then, the exterior acoustic boundary-value problem (1) has a unique radiating solution u^+ which belongs to the space

$$H_{\text{loc}}^1(\overline{\Omega}^+) := \left\{ v \in \mathcal{D}'(\Omega^+)/\psi v \in H^1(\Omega^+), \quad \forall \psi \in \mathcal{D}(\mathbb{R}^3) \right\}.$$

The first main difficulty arising in the numerical solution of the exterior problem (1) is related to the unboundedness of the computational domain Ω^+ . Integral equations method is one of the principal tools to overcome this concern. This approach is based on the classical potential theory [23]. It allows to reformulate problem (1) equivalently as an integral equation on the finite surface Γ . Let us recall the main notions. We first introduce the functional spaces [43]

$$H_-^1(\Delta) := H^1(\Delta, \overline{\Omega}^-) := \left\{ u \in H^1(\overline{\Omega}^-); \Delta u \in L^2(\overline{\Omega}^-) \right\},$$

$$H_+^1(\Delta) := H_{\text{loc}}^1(\Delta, \overline{\Omega}^+) := \left\{ u \in H_{\text{loc}}^1(\overline{\Omega}^+); \Delta u \in L_{\text{loc}}^2(\overline{\Omega}^+) \right\}.$$

For $u \in H_{\pm}^1(\Delta)$, the exterior (+) and interior (−) trace operators of order j ($j = 0$ or 1) can be defined by

$$\begin{aligned} \gamma_0^{\pm} : H_{\pm}^1(\Delta) &\rightarrow H^{1/2}(\Gamma) & \gamma_1^{\pm} : H_{\pm}^1(\Delta) &\rightarrow H^{-1/2}(\Gamma) \\ u^{\pm} &\mapsto \gamma_0^{\pm} u^{\pm} = u^{\pm}|_{\Gamma}, & u^{\pm} &\mapsto \gamma_1^{\pm} u^{\pm} = \partial_{\mathbf{n}} u^{\pm}|_{\Gamma}. \end{aligned} \quad (2)$$

We have the Green's representation theorem [23,40].

Theorem 2. *Let $(u^-, u^+) \in H^1(\Omega^-) \times H_{\text{loc}}^1(\overline{\Omega}^+)$ satisfying*

$$\begin{cases} \Delta u^- + k^2 u^- = 0, & \text{in } \Omega^-, \\ \Delta u^+ + k^2 u^+ = 0, & \text{in } \Omega^+, \\ u^+ \text{ outgoing wave.} \end{cases}$$

Then, we have

$$\mathcal{D}(\gamma_0^- u^-)(\mathbf{x}) + \mathcal{L}(\gamma_1^- u^-)(\mathbf{x}) = \begin{cases} u^-(\mathbf{x}), & \mathbf{x} \in \Omega^-, \\ 0, & \mathbf{x} \in \Omega^+ \end{cases}, \quad (3)$$

$$-\mathcal{D}(\gamma_0^+ u^+)(\mathbf{x}) - \mathcal{L}(\gamma_1^+ u^+)(\mathbf{x}) = \begin{cases} 0, & \mathbf{x} \in \Omega^-, \\ u^+(\mathbf{x}), & \mathbf{x} \in \Omega^+, \end{cases} \quad (4)$$

where the respective single-layer and double-layer potentials \mathcal{L} and \mathcal{D} are given by

$$\mathcal{L}p(\mathbf{x}) := \int_{\Gamma} G(\mathbf{x}, \mathbf{y}) p(\mathbf{y}) d\Gamma(\mathbf{y}), \quad \mathbf{x} \notin \Gamma, \quad (5)$$

$$\mathcal{D}\varphi(\mathbf{x}) := - \int_{\Gamma} \partial_{\mathbf{n}(\mathbf{y})} G(\mathbf{x}, \mathbf{y}) \varphi(\mathbf{y}) d\Gamma(\mathbf{y}), \quad \mathbf{x} \notin \Gamma, \quad (6)$$

for $(p, \varphi) \in H^{-1/2}(\Gamma) \times H^{1/2}(\Gamma)$, and G is the fundamental solution of the Helmholtz equation in \mathbb{R}^3

$$G(\mathbf{x}, \mathbf{y}) = \frac{1}{4\pi} \frac{e^{ik|\mathbf{x}-\mathbf{y}|}}{|\mathbf{x}-\mathbf{y}|}, \quad \mathbf{x} \neq \mathbf{y}.$$

The Cauchy data $(\gamma_0^+ u^+, \gamma_1^+ u^+)$ become the new unknowns. The acoustic wave u^+ in Ω^+ is uniquely determined from the knowledge of these two surface fields. To obtain an integral equation on the boundary Γ to find these fields, we need the trace formulae of the two potentials (see for instance [43]).

Proposition 1. *The first and second traces on Γ of the single-layer and the double-layer potentials \mathcal{L} and \mathcal{D} are given by*

$$\begin{cases} \gamma_0^- \circ \mathcal{L} = \gamma_0^+ \circ \mathcal{L} = L \\ \gamma_1^- \circ \mathcal{L} = -\frac{1}{2} + N \\ \gamma_1^+ \circ \mathcal{L} = \frac{1}{2} + N \end{cases} \quad \begin{cases} \gamma_0^- \circ \mathcal{D} = -\frac{1}{2} + M \\ \gamma_0^+ \circ \mathcal{D} = \frac{1}{2} + M \\ \gamma_1^- \circ \mathcal{D} = \gamma_1^+ \circ \mathcal{D} = D \end{cases}$$

where I is the identity operator and L , N , M and D the four elementary boundary integral operators expressed, for all $\mathbf{x} \in \Gamma$, by

$$\begin{aligned} Lp(\mathbf{x}) &:= \int_{\Gamma} G(\mathbf{x}, \mathbf{y}) p(\mathbf{y}) d\Gamma(\mathbf{y}), \\ Np(\mathbf{x}) &:= \int_{\Gamma} \partial_{\mathbf{n}(\mathbf{x})} G(\mathbf{x}, \mathbf{y}) p(\mathbf{y}) d\Gamma(\mathbf{y}), \\ M\varphi(\mathbf{x}) &:= - \int_{\Gamma} \partial_{\mathbf{n}(\mathbf{y})} G(\mathbf{x}, \mathbf{y}) \varphi(\mathbf{y}) d\Gamma(\mathbf{y}), \\ D\varphi(\mathbf{x}) &:= -\partial_{\mathbf{n}(\mathbf{x})} \int_{\Gamma} \partial_{\mathbf{n}(\mathbf{y})} G(\mathbf{x}, \mathbf{y}) \varphi(\mathbf{y}) d\Gamma(\mathbf{y}). \end{aligned} \quad (7)$$

The Helmholtz representation (3), (4) allows the derivation of several integral equations, each with its own mathematical properties (see for instance [9,23,24,40]). To this end, first or second trace is applied to (3), (4) and satisfaction of the boundary condition leads to an integral equation posed on Γ .

3. Combined boundary integral equation formulations

This section presents the integral equation formulations that we compare in this paper: the classical Combined Field Integral Equation (CFIE) [33] and an OSRC-preconditioned CFIE proposed in [7].

3.1. CFIE

To solve the exterior sound-hard acoustic scattering problem (1), we consider the well-known CFIE: find the physical unknown $\varphi = -\gamma_0^+(u^+ - u^{\text{inc}}) \in H^{1/2}(\Gamma)$ solution to

$$\left(\frac{I}{2} + M + \eta D\right)\varphi = -\gamma_0^+ u^{\text{inc}} - \eta \gamma_1^+ u^{\text{inc}}, \quad \text{on } \Gamma, \quad (8)$$

with a coupling complex parameter η . This integral equation is constructed as a linear combination of the Magnetic Field Integral Equation (MFIE)

$$\left(\frac{I}{2} + M\right)\varphi = -\gamma_0^+ u^{\text{inc}}, \quad \text{on } \Gamma,$$

and the Electric Field Integral Equation (EFIE)

$$D\varphi = -\gamma_1^+ u^{\text{inc}}, \quad \text{on } \Gamma.$$

We have the following existence and uniqueness result [14].

Proposition 2. *Consider Γ a Lipschitz continuous surface. The operator*

$$\frac{I}{2} + M + \eta D,$$

defines an isomorphism from $H^{1/2}(\Gamma)$ onto $H^{-1/2}(\Gamma)$ for all $k > 0$ provided $\Im(\eta) \neq 0$. Under this condition, the CFIE (8) is uniquely solvable in $H^{1/2}(\Gamma)$ for all frequency $k > 0$.

The reference CFIE considered in the paper is defined on Γ by

$$[(1 - \alpha) \frac{i}{k} (\frac{I}{2} + M) + \alpha D]\varphi = -(1 - \alpha) \frac{i}{k} \gamma_0^+ u^{\text{inc}} - \alpha \gamma_1^+ u^{\text{inc}}, \quad (9)$$

setting $\eta = -\frac{\alpha}{(1-\alpha)} ik$ with $\alpha \in \mathbb{R} \setminus \{0, 1\}$.

3.2. OSRC-preconditioned CFIE

In terms of numerical iterative resolution, even if CFIE (9) has the good property of being uniquely solvable, this equation is a Fredholm integral equation of the first-kind and does not provide an interesting spectral behavior (see Section 6). In fact, it involves the first-order, strongly singular and non-compact operator D . To expect an eigenvalue clustering and hence a fast convergence of iterative solvers, the idea consists in composing the EFIE (operator D) with a regularizing operator of the

opposite order before combining it with the MFIE. We adopt the approach of Antoine and Darbas [6,7]. Consider the exact exterior Neumann-to-Dirichlet (NtD) map

$$\begin{aligned} V^{\text{ex}} : H^{-1/2}(\Gamma) &\rightarrow H^{1/2}(\Gamma) \\ \gamma_1^+ u^+ &\mapsto \gamma_0^+ u^+ = V^{\text{ex}} \gamma_1^+ u^+. \end{aligned} \quad (10)$$

The NtD operator V^{ex} is a non-local pseudodifferential operator of order -1 . The following integral relation holds

$$-V^{\text{ex}} D = \frac{I}{2} - M, \quad \text{on } \Gamma,$$

and then

$$\frac{I}{2} + M - V^{\text{ex}} D = I, \quad \text{on } \Gamma.$$

In this ideal configuration, the solution $\varphi = -\gamma_0^+ u^{\text{inc}} + V^{\text{ex}} \gamma_1^+ u^{\text{inc}} \in H^{1/2}(\Gamma)$ is computed directly. However, as well-known, an expression of the exact NtD is not available for a general surface Γ . Instead, an approximation \tilde{V} of V^{ex} is introduced to construct the OSRC-preconditioned CFIE: find $\varphi = -\gamma_0^+ (u^+ - u^{\text{inc}}) \in H^{1/2}(\Gamma)$ such that

$$\left(\frac{I}{2} + M - \tilde{V} D \right) \varphi = -\gamma_0^+ u^{\text{inc}} + \tilde{V} \gamma_1^+ u^{\text{inc}}, \quad \text{on } \Gamma. \quad (11)$$

An efficient approximation \tilde{V} is derived in [8] according to On-Surface Radiation Conditions (OSRC) method [4,5,34,38]

$$\tilde{V} = \frac{1}{ik} \left(1 + \frac{\Delta_\Gamma}{k_\varepsilon^2} \right)^{-1/2}, \quad (12)$$

where the operator Δ_Γ is the Laplace–Beltrami operator over the surface Γ and the parameter $k_\varepsilon = k + i\varepsilon$ is complex-valued. The small damping parameter $\varepsilon \in \mathbb{R}^*$ is introduced to regularize the square-root operator in the transition zone of grazing modes. A suitable choice of ε has been determined in [25]: $\varepsilon = 0.4k^{1/3}R^{-2/3}$ where R is the radius of the smallest sphere containing Ω . We discuss the implementation of the operator \tilde{V} in Section 4.2. We have the following existence and uniqueness result:

Proposition 3. Consider Γ a smooth surface, the OSRC-preconditioned CFIE (11) is uniquely solvable in $H^{1/2}(\Gamma)$ for any wavenumber k and any damping parameter $\varepsilon \neq 0$.

The proof [25] relies on two simple ingredients: the symbolic calculus and the Fredholm alternative. Indeed, the operator \tilde{V} has the desired regularizing effect on the operator D and the preconditioned CFIE (11) is a second-kind Fredholm integral equation expressed by

$$\frac{I}{2} + M - \tilde{V} D = \left(\frac{1}{2} + \frac{k_\varepsilon}{2k} \right) I + C, \quad (13)$$

where C is a compact operator. In the case of a non-smooth boundary, some tools and regularization techniques are given in [21,14] for other combined field equations. These tools are not suitable for our Eq. (11) in the case of Lipschitz boundaries and would require more investigation.

4. Discretization and implementation

We describe in this section our strategy for the computation of the proposed preconditioned integral equations.

4.1. Discretization and iterative resolution

For the numerical resolution, we consider a classical \mathbb{P}_1 boundary finite element discretization [19]. The surface mesh is denoted by Γ_h . We define the total number of triangles by N_T and the total number of vertices by N_V . Let us designate by $n_\lambda = \lambda/h_{\max}$ the density of discretization points per wavelength where h_{\max} is the maximal length of the edges of the triangles. The OSRC-preconditioned CFIE uses the CFIE integral operators and in addition only some differential operators involved in the OSRC approach. The discretization of the later gives rise to sparse matrices. However, as well-known, the discretization of integral operators leads to dense matrices. Moreover, the integrals involve singular kernels. To deal with the hypersingular integral operator D , we have considered the following expression [43]

$$(D\varphi, \psi) = - \int_\Gamma \int_\Gamma G(\mathbf{x}, \mathbf{y}) [k^2 \varphi(\mathbf{y}) \psi(\mathbf{x}) \mathbf{n}(\mathbf{x}) \cdot \mathbf{n}(\mathbf{y}) - \mathbf{curl}_\Gamma \varphi(\mathbf{y}) \cdot \mathbf{curl}_\Gamma \psi(\mathbf{x})] d\Gamma(\mathbf{y}) d\Gamma(\mathbf{x}),$$

that involves only weakly singular kernels. The singularities are then evaluated using a technique based on singular changes of variables related to Duffy transformation [31].

Let us denote by $[A] \in \mathbb{C}^{N_V \times N_V}$ the matrix associated with the linear discretization of a given integral operator A . We solve the different dense non-symmetric linear systems with the iterative solver GMRES [47] with no restart in order to have a precise idea of the impact of the OSRC technique on the convergence of the solver. The uses of the restart (with 20, 30 or 50 inner iterations) that we performed with the unit sphere and the cube with cavity, considered for the numerical tests, were not successful for the CFIE operator. In the numerical results, by “iterations”, we then always refer to “inner iterations”. Moreover, we always precondition the GMRES by the mass matrix. At each step of the solver, the solution of (11) needs the computation of

$$\mathbf{Y} = \left(\frac{[I]}{2} + [M] - [\tilde{V}][D] \right) \mathbf{X},$$

with $\mathbf{X}, \mathbf{Y} \in \mathbb{C}^{N_V}$. For the sake of efficiency

- a sparse direct solver is used to apply the OSRC preconditioner $[\tilde{V}]$ (see Section 4.2),
- the single-level Fast Multipole Method is chosen to evaluate the dense matrix–vector products involving $[M]$ and $[D]$ (see Section 4.3).

4.2. Discretization of the OSRC preconditioner

Let us explain how to compute accurately the square-root needed for the non-local pseudodifferential operator \tilde{V} . A Padé paraxial approximation of order N_p of the square-root operator is used: a rotating branch-cut technique [41,8],

$$\left(1 + \frac{\Delta_\Gamma}{k_e^2} \right)^{1/2} \approx C_0 + \sum_{j=1}^{N_p} \frac{A_j}{k_e^2} \Delta_\Gamma \left(1 + \frac{B_j}{k_e^2} \Delta_\Gamma \right)^{-1},$$

where C_0 , A_j and B_j , $1 \leq j \leq N_p$ are complex coefficients. They depend on the rotation angle θ_p of the usual branch-cut $\{z \in \mathbb{R}; z < -1\}$ of the square-root $z \mapsto \sqrt{1+z}$. In this paper, we always take $\theta_p = \pi/3$. The unique solvability of the OSRC-preconditioned CFIE (cf. Proposition 3) remains true even when we use such Padé approximants to localize the square-root operator. The proof based on symbolic calculus can be easily adapted.

Specifically, the matrix–vector product $\mathbf{Y} = [\tilde{V}]\mathbf{X}$ is realized by first solving N_p Helmholtz-type sparse linear systems

$$\left(\frac{B_j}{k_e^2} [\Delta_\Gamma] + [I] \right) \mathbf{X}_j = [I] \mathbf{X}, \quad j = 1, \dots, N_p,$$

and in a second step by solving the problem

$$\left([I] + \frac{[\Delta_\Gamma]}{k_e^2} \right) \mathbf{Y} = \frac{1}{ik} \left(C_0 [I] \mathbf{X} + \sum_{j=1}^{N_p} \frac{A_j}{k_e^2} [\Delta_\Gamma] \mathbf{X}_j \right).$$

The matrix $-\Delta_\Gamma$ represents the rigidity matrix on Γ_h . The operator \tilde{V} has desirable advantages for preconditioners: sparse structure, ease of implementation and low additional computational cost (see Section 7). We use MUMPS library (MULTifrontal Massively Parallel sparse direct Solver – <http://mumps.enseeiht.fr/>) to take advantage of the sparse structure of $[\tilde{V}]$.

4.3. Single-level FMM

In order to reduce the computation cost related to the dense matrices, the FMM splits partially the interactions between both the column and row entries of the matrices. This is done thanks to a separation of variables \mathbf{x} and \mathbf{y} in the Green’s kernel $G(\mathbf{x}, \mathbf{y})$: the degrees of freedom are contained in boxes (called FMM boxes below – see Fig. 1), and the interaction between two degrees of freedom is replaced by a succession of translations through the centers of the boxes that contain the degrees of freedom. In a single-level FMM, only boxes of a same size, of a same level of an oc-tree are considered. In a multilevel FMM, boxes from different levels are involved. The FMM strategy is illustrated in Fig. 2.

In this paper, the single-level FMM that we consider is based on the Gegenbauer series and Funk–Hecke formula. For instance, an efficient calculation of the matrix–vector product $[L]\mathbf{X}$ with matrix

$$[L]_{ij} = \int_\Gamma \int_\Gamma G(\mathbf{x}, \mathbf{y}) \varphi_j(\mathbf{y}) \varphi_i(\mathbf{x}) d\Gamma(\mathbf{y}) d\Gamma(\mathbf{x}), \quad i, j = 1, \dots, N_V,$$

can be expressed thanks to such an expansion for i far from j :

$$[L]_{ij} \approx \sum_{p=1}^P c_p \sum_{B/B \cap \text{supp} \varphi_i \neq \emptyset} g_{i,B}^{(p)} \sum_{\substack{\sim \\ B/B \cap \text{supp} \varphi_j \neq \emptyset}} \mathcal{T}_{B,B}^{(p)} f_{j,B}^{(p)},$$

with

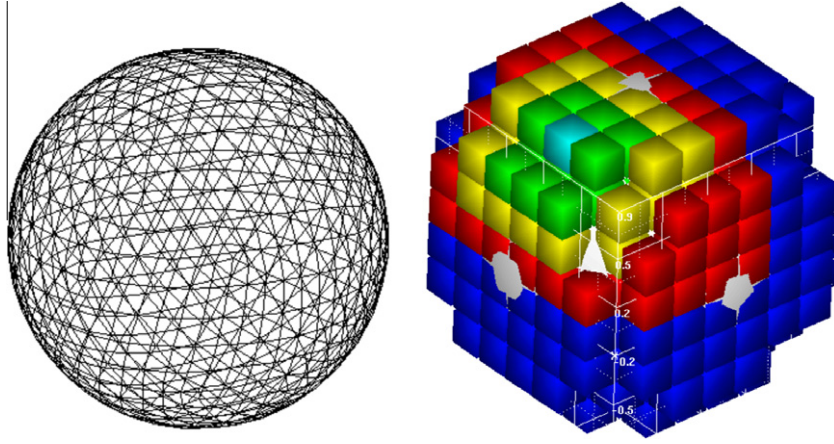


Fig. 1. FMM boxes: a mesh (left) and corresponding FMM boxes (right).

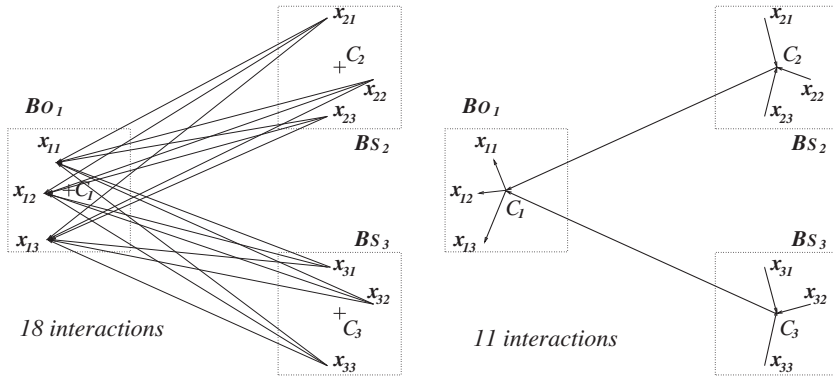


Fig. 2. FMM strategy: without FMM on left, with FMM on right.

$$c_p = \frac{ik}{(4\pi)^2} w_p,$$

$$g_{i,B}^{(p)} = \int_{B \cap \text{supp} \varphi_i} e^{ik \langle s_p, \mathbf{x} - C_B \rangle} \varphi_i(\mathbf{x}) d\Gamma(\mathbf{x}),$$

$$\tilde{f}_{j,B}^{(p)} = \int_{B \cap \text{supp} \varphi_j} e^{-ik \langle s_p, \mathbf{y} - C_B \rangle} \varphi_j(\mathbf{y}) d\Gamma(\mathbf{y}),$$

and $\mathcal{T}_{B,B}^{(p)}$ is the translation operator from the FMM box \tilde{B} to the FMM box B given by the expression

$$\mathcal{T}_{B,B}^{(p)} = \sum_{\ell=1}^L (-i)^\ell (2\ell + 1) h_\ell^{(1)}(k|C_B - C_{\tilde{B}}|) P_\ell(\cos(s_p, C_B - C_{\tilde{B}})), \quad (14)$$

where w_p , s_p are the quadrature weights and points for the integration on the unit sphere involved in the Funk–Hecke formula. The summation “ $\sum_{p=1}^P$ ” comes from the discretization of the Funk–Hecke formula while the summation “ $\sum_{\ell=1}^L$ ” is a truncation of the Gegenbauer series. Moreover, C_B denotes the center of the FMM box B , $h_\ell^{(1)}$ is the spherical Hankel function of the first kind of degree ℓ , and P_ℓ is the Legendre polynomial of degree ℓ . The parameters L and P are estimated thanks to the empirical formula [35] $L = kd + C(kd)^3$, and the choice of the discretization of the unit sphere such that $P = (L + 1)(2L + 1)$, where d is the diameter of the FMM boxes.

This leads to an algorithm of complexity which is $N_V^{3/2}$ for a single-level FMM and $N_V \ln^2 N_V$ for a multilevel FMM. For more details on the FMM, we refer for example to the papers [20,28,29,35,45]. This choice leads to a FMM which is known to be unstable at “low-frequency regimes”. This occurs for any frequency when the mesh density n_λ is large compared to the usual value $n_\lambda = 10$. This comes from the translation operator $\mathcal{T}_{B,B}^{(p)}$ (14) which sums Hankel functions. In the Gegenbauer series, the diverging behavior of the Hankel function is controlled by the converging Bessel function. But the considered FMM expan-

sion separates the Hankel function such that the translation operator (14) becomes unstable at low-frequency regimes. In this paper, we effectively meet with this issue (cf. Remark 1).

5. Presentation of the test geometries

For the numerical results, we have considered several geometries for different purposes as presented below. The geometries were generated using Gmsh [32].

First, the unit sphere enables us to validate the code by comparison with the analytical solution.

A second concern is the consideration of domains with cavity. We have intensively studied a cube with cavity that takes inspiration in the 2-D trapping domain defined by Betcke and Spence [11] (cf. Fig. 3, left). This 3-D geometry is the cube $[-1, 1]^3$ with the rectangular cavity $[0, 1] \times [-\pi/10, \pi/10] \times [-\pi/10, \pi/10]$, shown in Fig. 3 (right). A second cavity domain consists in a 3-D spherical trapping object given in Fig. 4 (left), generated by the revolution around the X-axis of a 2-D C-shape contour (Fig. 4, right). The 2-D contour is defined with the help of four circles; for each of them, the couple (center, radius) is respectively $(O, 1.4)$, $(O, 1)$, $(A, 0.2)$, $(B, 0.2)$. The two last centers are given by applying rotations of angles $\pi/5$ and $-\pi/5$ and center $O = (0, 0)$ to the point $(0, 1.2)$.

The cone-sphere (Fig. 5, left) and the submarine offer configurations with singularities. The cone-sphere is based on the unit sphere and has the apex located at the point $(5, 0, 0)$. Moreover, for this geometry, the cone and the sphere are tangent to each other at the interface. As a last example, we consider the geometry of a submarine shown in Fig. 5 (right). The characteristic length are: length = 43 m, thickness ≈ 4 –7 m, high ≈ 4 –7 m. This example presents a sharp and irregular shape at the back (around point $(43, 0, 0)$), and is characterized by very large length.

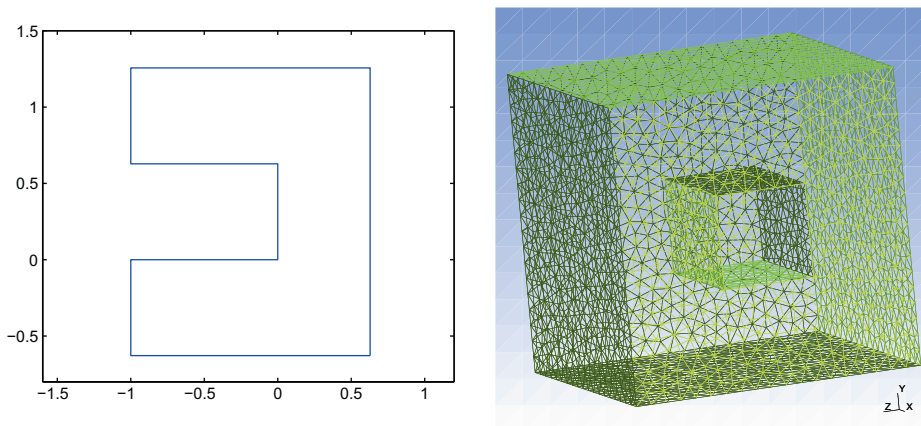


Fig. 3. 2-D and 3-D “rectangular” cavities.

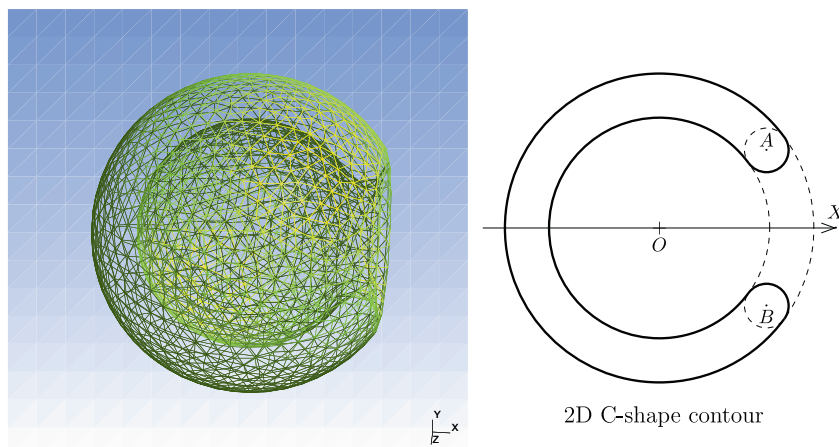


Fig. 4. Sphere with cavity and its 2D generator.

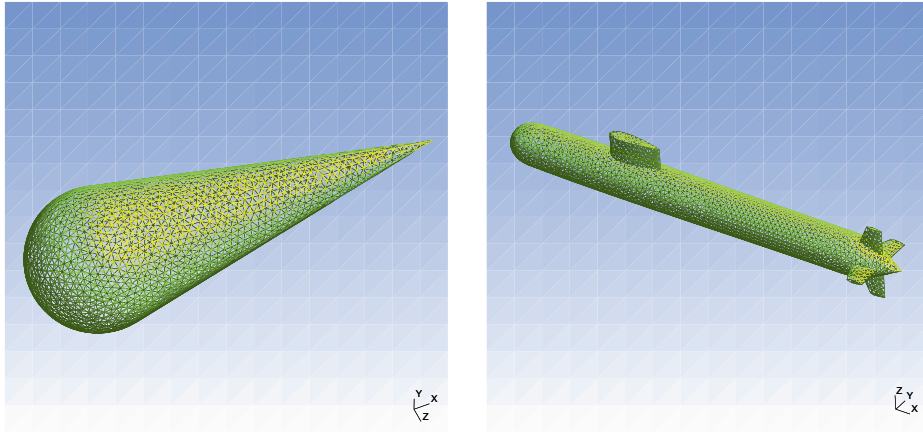


Fig. 5. Left: cone-sphere – right: submarine.

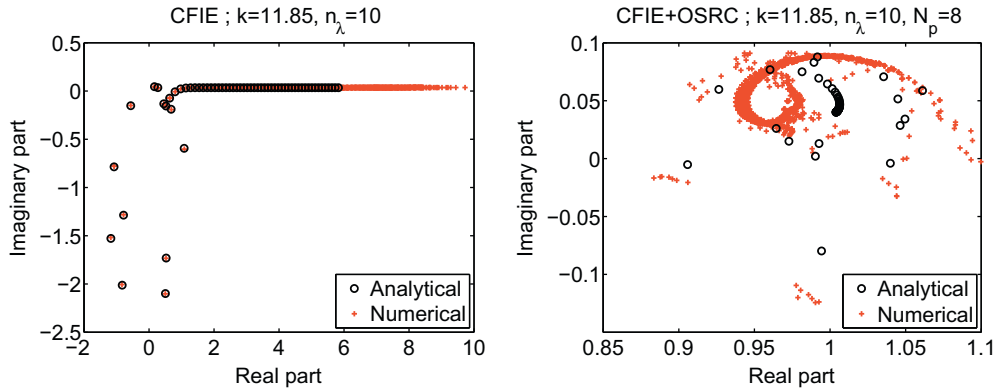


Fig. 6. Unit sphere: distribution of the eigenvalues, $k = 11.85$, $n_\lambda = 10$.

6. Spectral analysis

In order to analyze the convergence properties of the GMRES algorithm for solving the usual and OSRC-preconditioned CFIEs (9) and (11), let us observe previously in this section the eigenvalue behavior of the involved integral operators. To this end, we use a code implemented with the library MELINA++,¹ and the library ARPACK++.² MELINA++ is a finite element (FE) library that provides the FE discretization of the integral operators and standard differential operators. To compute numerical eigenvalues, ARPACK++ implements the “Implicit Restarted Arnoldi Method” (IRAM), which combines Arnoldi factorizations with an implicitly shifted QR method.

6.1. Spherical case

We consider the unit sphere as the scatterer. Spherical harmonics form a basis of eigenvectors for the elementary integral operators. Explicit expressions of the eigenvalues of the CFIE operators are known [3,7,25,36]. In the case of the OSRC-preconditioned CFIE, we know such an analytic expression either with the exact square-root operator in \tilde{V} (cf. (12)) or with the complex Padé approximation (cf. Section 4.2) for the localization of \tilde{V} . In this section, we designate by “analytical eigenvalues” the exact eigenvalues obtained with the exact square-root operator and by “Padé-analytical” the ones obtained considering Padé approximants. The eigenvalues computed with our code based on a BEM discretization are called “numerical eigenvalues”.

In Fig. 6, we compare the analytical and the numerical eigenvalues of the CFIE integral operators for the wavenumber $k = 11.85$, with the mesh density $n_\lambda = 10$. For the numerical results, we choose the Padé order $N_p = 8$.

¹ <http://anum-maths.univ-rennes1.fr/melina/>

² <http://www.ime.unicamp.br/~chico/arpac++/>

The analytical eigenvalues of the CFIE operator coincide with the numerical ones. The numerical eigenvalues of the OSRC-preconditioned operator are well clustered at a point near to $(1,0)$ which is the accumulation point of the analytical ones. Now, let us observe how the Padé approximation impacts on the clustering of the eigenvalues. To this aim, for different Padé orders, we compare the Padé-analytical eigenvalues to the analytical ones in Fig. 7, and the numerical eigenvalues to the Padé-analytical ones in Fig. 8. In both Figs. 7 and 8, the Padé-analytical eigenvalues are the same.

For both the Padé-analytical and numerical eigenvalues, more precise is the Padé approximation, better is the clustering of the eigenvalues around the point $(1,0)$. The figures show a spiral curve which is absorbed by the accumulation point progressively when the Padé order N_p increases. This curve has been an interesting tool to determine the influence of the Padé approximation on the accuracy of the resolution strategy. Indeed, the Padé approximation presents two critical points: when z is close to -1 and when z is large. When k becomes large, some eigenvalues of the discretized operator $[\Delta_\Gamma]/k_\epsilon^2$ may be close to -1 ; when n_λ is large, some eigenvalues of $[\Delta_\Gamma]/k_\epsilon^2$ become large. However, this phenomenon does not really affect the

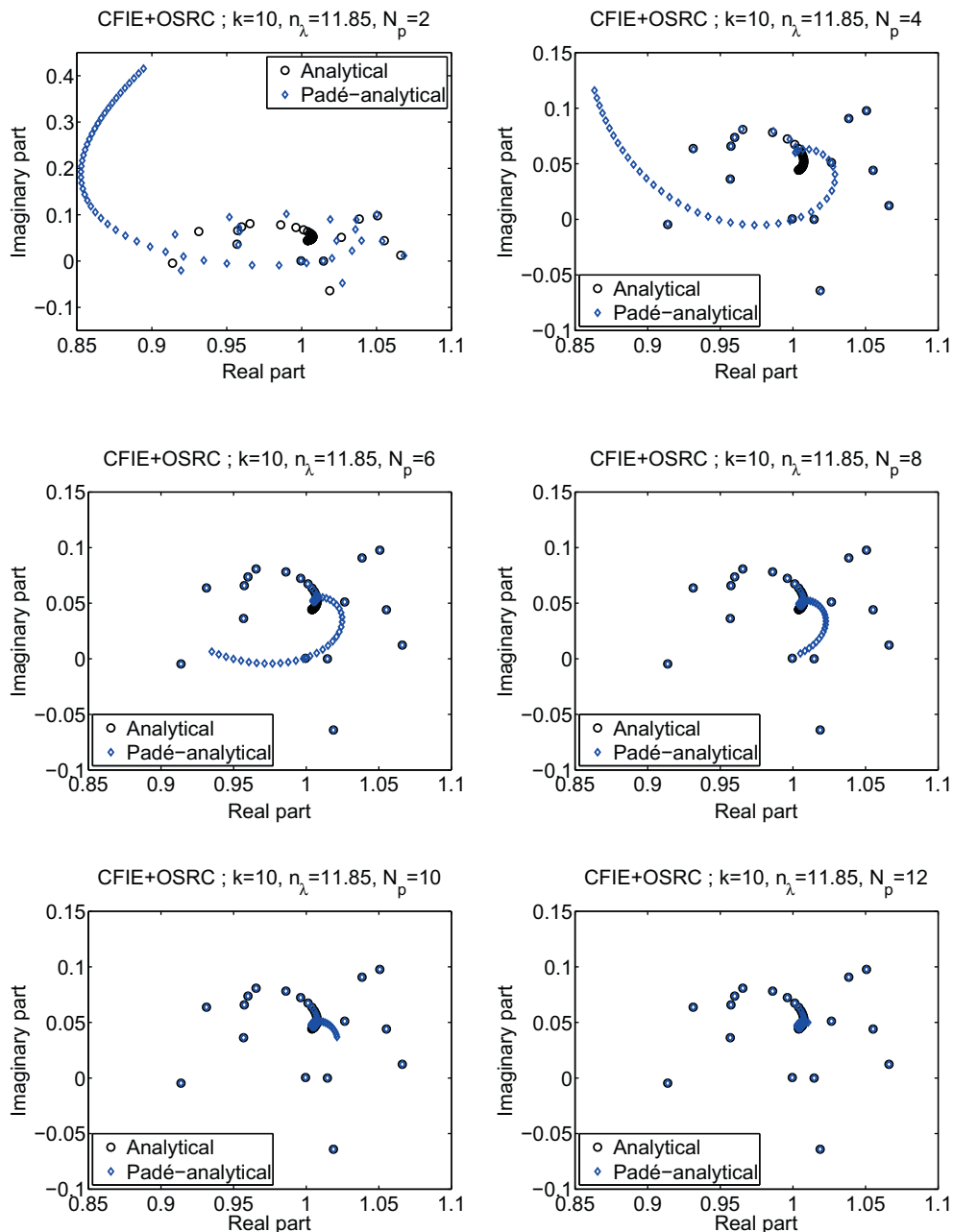


Fig. 7. Unit sphere: distribution of the analytical eigenvalues versus Padé order N_p , for $k = 10$, $n_\lambda = 11.85$.

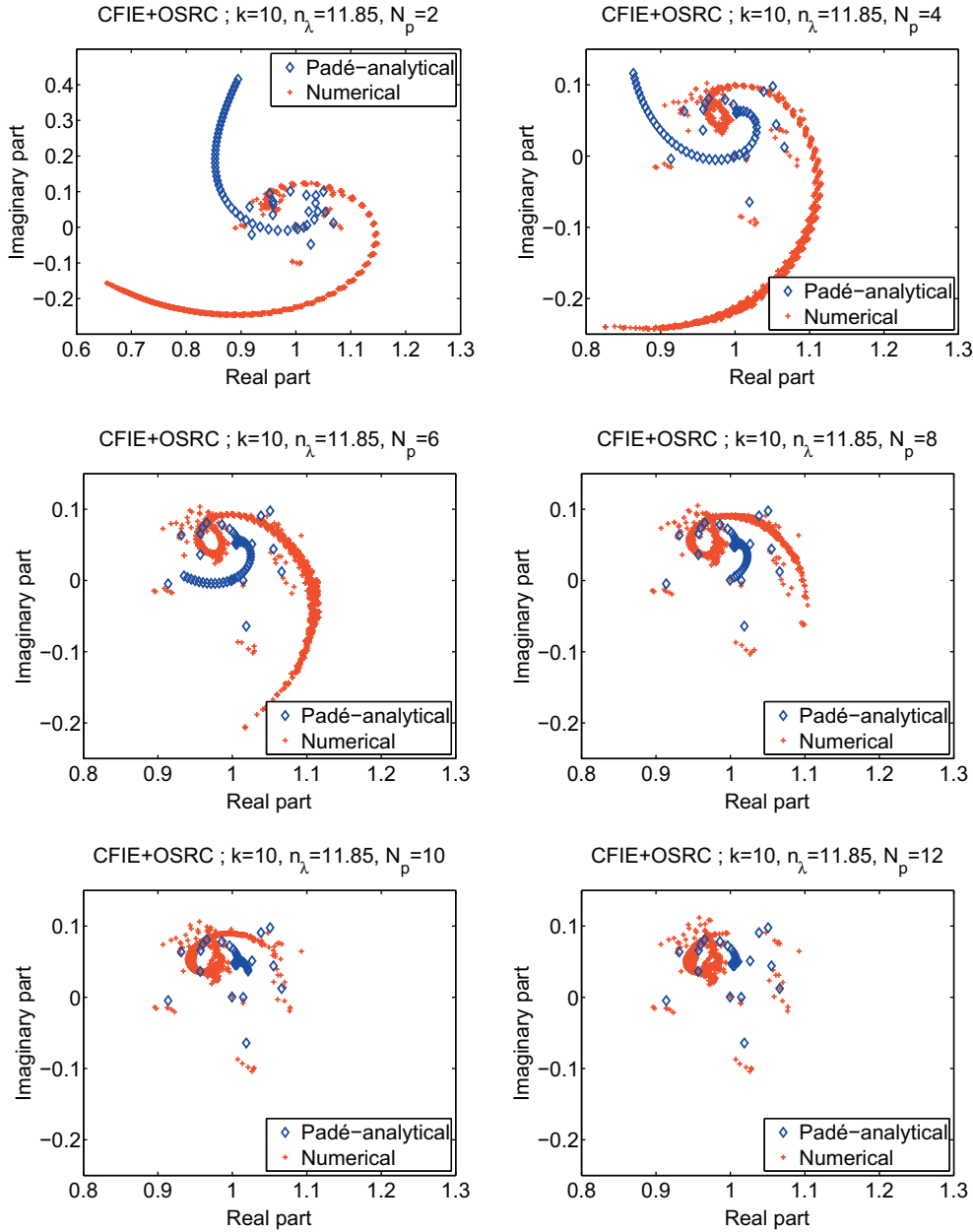


Fig. 8. Unit sphere: distribution of the eigenvalues versus Padé order N_p , for $k = 10$, $n_\lambda = 11.85$.

condition number in our configurations (see Fig. 9). As we can see, the condition number of the OSRC-preconditioned CFIE remains between 1.2 and 1.7 independently of the Padé order, the frequency and the mesh density so far. More precisely, in Fig. 9(b) and (c), this condition number lies between 1.2 and 1.31. This is not the case for the CFIE. The linear dependance of the CFIE condition number on n_λ is related to the dispersion of the eigenvalues in the elliptic part. These eigenvalues which lie on the real line $x = 0$ are associated with evanescent modes (high-order spatial modes). The dependance on k comes from the small-magnitude eigenvalues linked to a grazing mode.

6.2. Cavity domains

Several studies of the conditioning and spectral properties of the combined boundary integral equations exist in the canonical case when Γ is a circle or a sphere [37,36,2] since a complete theory of conditioning is available. Recent results [10,11] have been obtained for more general two-dimensional domains (convex, non-convex, polygon, starlike polygon,

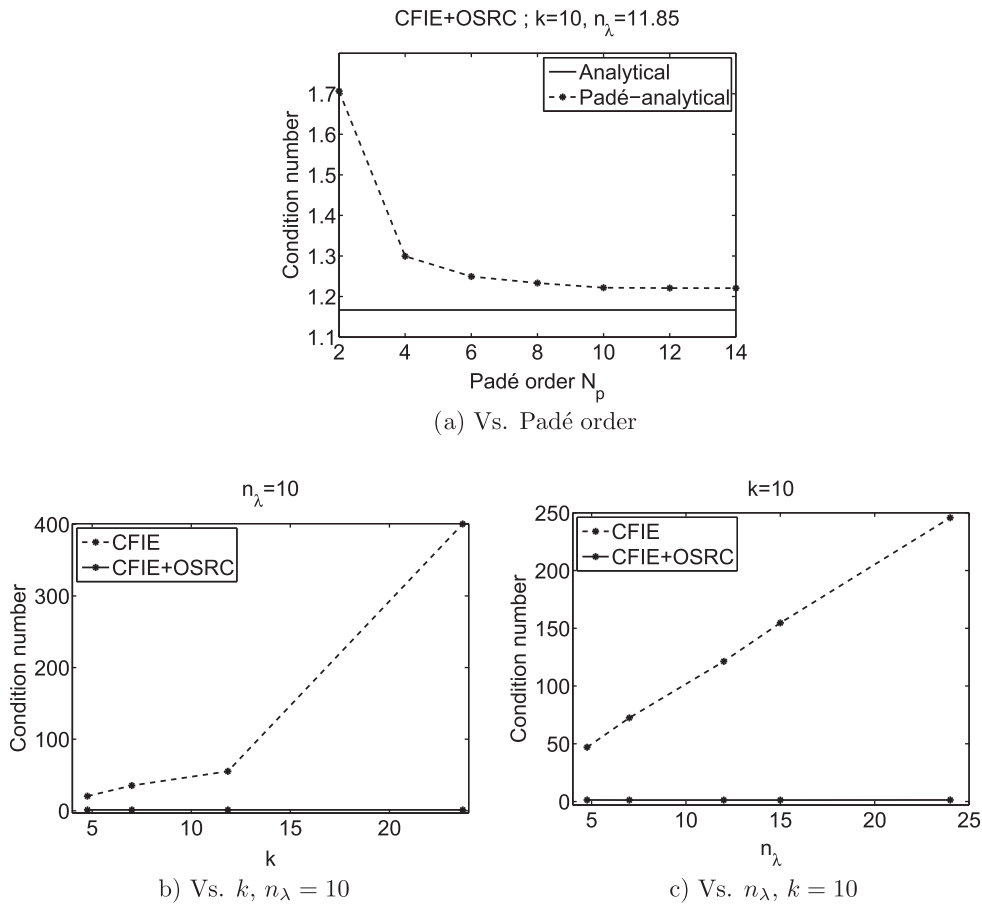


Fig. 9. Unit sphere: condition number.

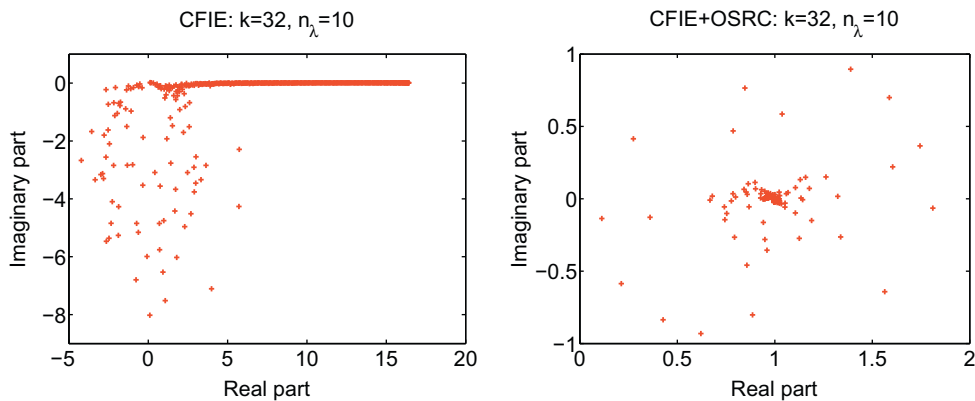


Fig. 10. 2-D open cavity: distribution of the eigenvalues ($k = 32, n_\lambda = 10$).

trapping domains) in the case of the acoustic sound-soft scattering problem. Let us note that the CFIE is a second-kind boundary integral equation for the sound-soft scattering problem. This is no more true for the sound-hard boundary condition. In [10], the derived estimates show that the condition number depends on the geometry of Γ , asymptotically as $k \rightarrow \infty$. For instance, the dependence on k is more pronounced for the case of a trapping obstacle than for the case of a circle or a square. Moreover, in [11], Betcke and Spence have conjectured numerically that the classical CFIE operator is coercive uniformly in k , for all sufficiently large wavenumbers k , for all non-trapping domains. Then, it is interesting to observe numerically how the OSRC-preconditioned CFIE behaves for such scattering objects in the sound-hard case.

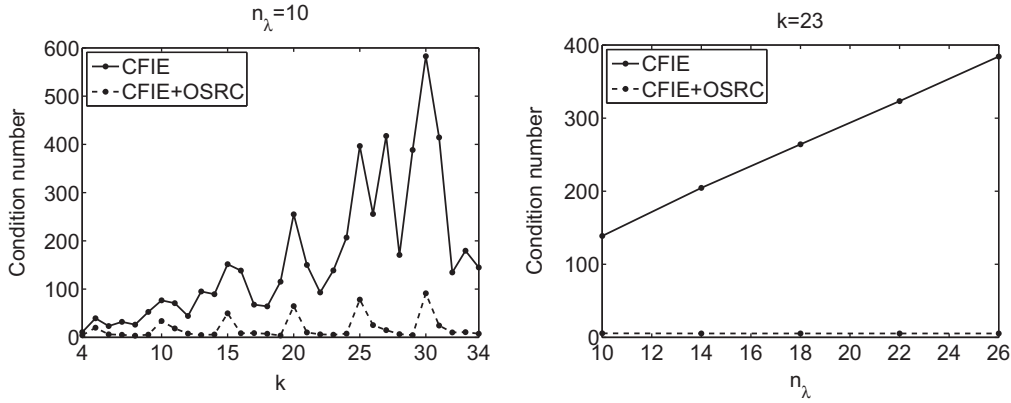


Fig. 11. 2-D open cavity: condition number of the CFIE operators.

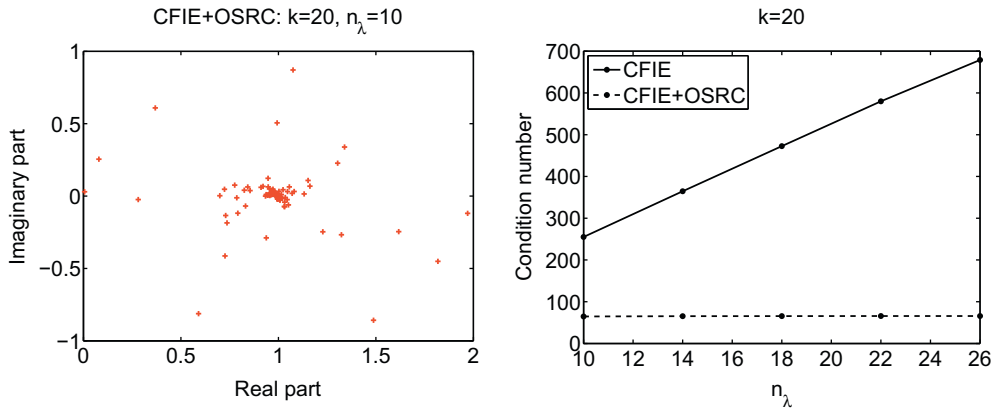


Fig. 12. 2-D open cavity: eigenvalues and condition number at resonance ($k = 20$).

First, we consider the two-dimensional trapping domain chosen by Betcke and Spence: an open cavity of width $\pi/5$ (cf. Fig. 3, left). We take $N_p = 8$ and $\theta_p = \pi/3$. We draw in Fig. 10 the eigenvalues of the CFIE operators taking $k = 32$ and $n_\lambda = 10$. Moreover, we plot in Fig. 11 the condition number of the two integral operators with respect to k (resp. n_λ) for $n_\lambda = 10$ (resp. $k = 23$). The eigenvalues of the CFIE operator are dispersed in the elliptic part. Moreover, small eigenvalues close to zero appear in the hyperbolic zone. Consequently, the condition number of the CFIE grows with both the mesh density n_λ and the increase of k . The dependence on n_λ comes from the large-magnitude eigenvalues, and the one on k from the small-magnitude eigenvalues. Note that most of the eigenvalues of the OSRC-preconditioned CFIE are again well clustered around the point (1, 0). However, there are a few small eigenvalues and at least one of them can be very close to zero at a resonance frequency (a multiple of 5, cf. [11]). We can observe the phenomenon in Fig. 12 for $k = 20$. This leads to a light dependence (compared to the CFIE) of the condition number on k accentuated at resonance frequencies.

Now, let us consider 3-D trapping domains, the cube with cavity (Fig. 3, right) and the sphere with cavity (Fig. 4). The first one is intensively considered as a 3-D generalization of the trapping domain by Betcke and Spence. The second domain confirms the results in a configuration where the cavity offers a wider hidden part. Figs. 13 and 14 show that the behavior of the eigenvalues is similar to what we already observed in the 2-D case: dispersion in the elliptic part and eigenvalues in a neighborhood of zero in the hyperbolic zone for the CFIE; clustering around a point near to (1, 0) for the OSRC-preconditioned CFIE. In Figs. 15 and 16, we compare the behavior of the condition number for both the CFIE and the OSRC-preconditioned CFIE versus the wavenumber k or versus the mesh density n_λ . First of all, let us look at the case of the CFIE. For a fixed wavenumber, as expected, we clearly see that the increase of the condition number is linked to the increase of the largest eigenvalue magnitude. We also check that the smallest-magnitude eigenvalues do not really vary and do not affect the condition number at fixed wavenumber. On the contrary, for a fixed mesh density, we see that the increase of the condition number is linked to the decrease of the smallest eigenvalue magnitude and we observe that the largest-magnitude eigenvalues do not really affect the condition number. In the case of these domains with cavity, which generate trapping phenomena, the OSRC-preconditioning does not completely vanish the dependencies on k and n_λ .

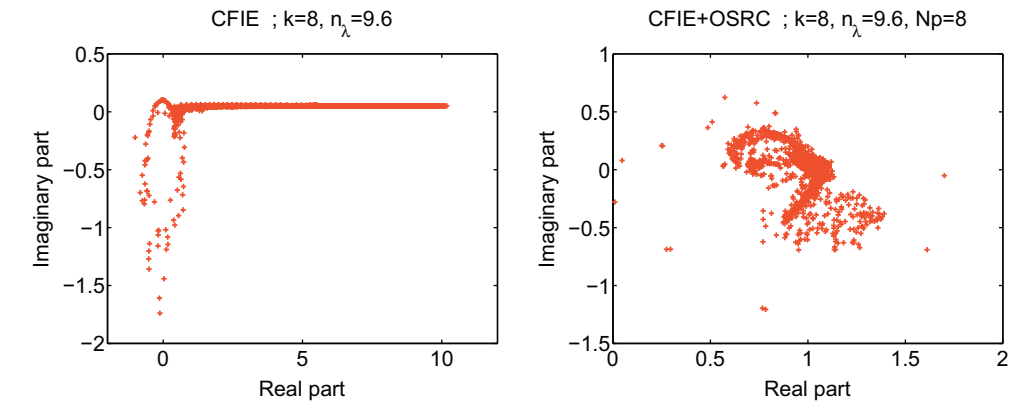


Fig. 13. Cube with cavity: distribution of the eigenvalues, $k = 8$, $n_\lambda = 9.6$, $N_p = 8$.

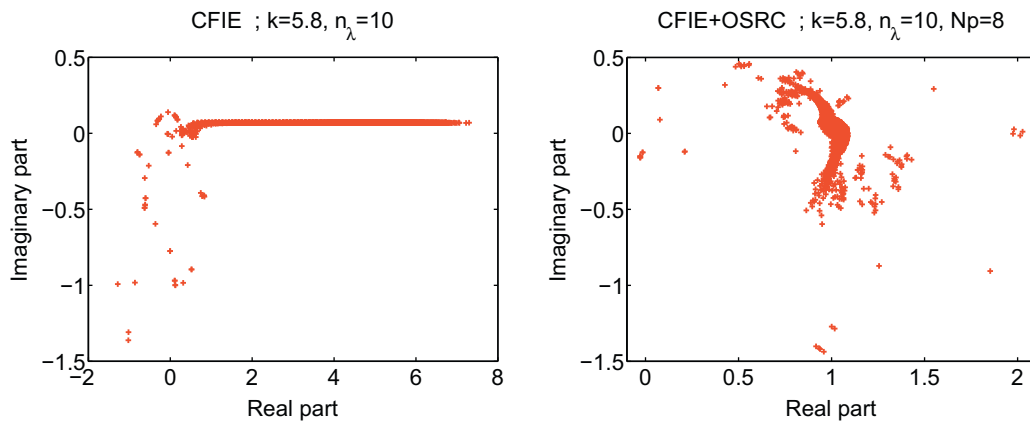


Fig. 14. Sphere with cavity: distribution of the eigenvalues, $k = 5.8$, $n_\lambda = 10$.

However, this approach strongly reduces these dependencies and the condition number is very small compared to the one of the CFIE: the condition number of the OSRC-preconditioned CFIE lies between 7 and 11 in Fig. 15 (left), and between 2 and 13 in Fig. 15 (right); moreover the largest (resp. smallest) eigenvalue magnitude of the OSRC-preconditioned CFIE is strongly smaller (resp. larger) than the one of the CFIE.

For the cube with cavity, in Fig. 17, we exhibit a resonance frequency around $k = 5.2$ where the OSRC-preconditioned CFIE has an eigenvalue that comes very close to zero. In Fig. 18 (left) we show the condition number versus k , in linear scale, where we considered numerous values of k , with four different meshes, whereas Fig. 18 (right) offers the same graph with a semi-logarithmic scale. To differentiate the different meshes, the curves are drawn alternatively using dashed and solid lines for the CFIE and using dashed and dotted lines for the OSRC-preconditioned CFIE. Fig. 18 (left) clearly indicates that the resonance effect is attenuated by the OSRC-preconditioning. Fig. 18 (right) offers another element on the behavior of the condition number versus n_λ : at the interface between two meshes (change of line style in the figure), we can observe that the values computed with a coarse mesh are smaller than the ones computed with a finer mesh. This is clear for the condition numbers of the CFIE. For the OSRC-preconditioned CFIE however, this phenomenon is much less visible and we can observe a very good transition from a mesh to another. The highlighted resonance frequencies are characterized by the presence of one or two eigenvalues close to zero: when two of them are near zero, they are close enough to interpret them as one eigenvalue with multiplicity 2. Moreover, it seems that this number of eigenvalues close to zero is the same with or without preconditioning (independently of the mesh for the case $k = 5.2$ where two meshes were used for this frequency). A comparable behavior is visible for the sphere with cavity in Fig. 19 (right).

Finally, in Fig. 19 (left), the condition number is considered versus the Padé order for the cube with cavity. The behavior is more significative than it is for the unit sphere considered previously. A first conclusion could be that the Padé order has to be chosen larger for domains with cavity than for the sphere.

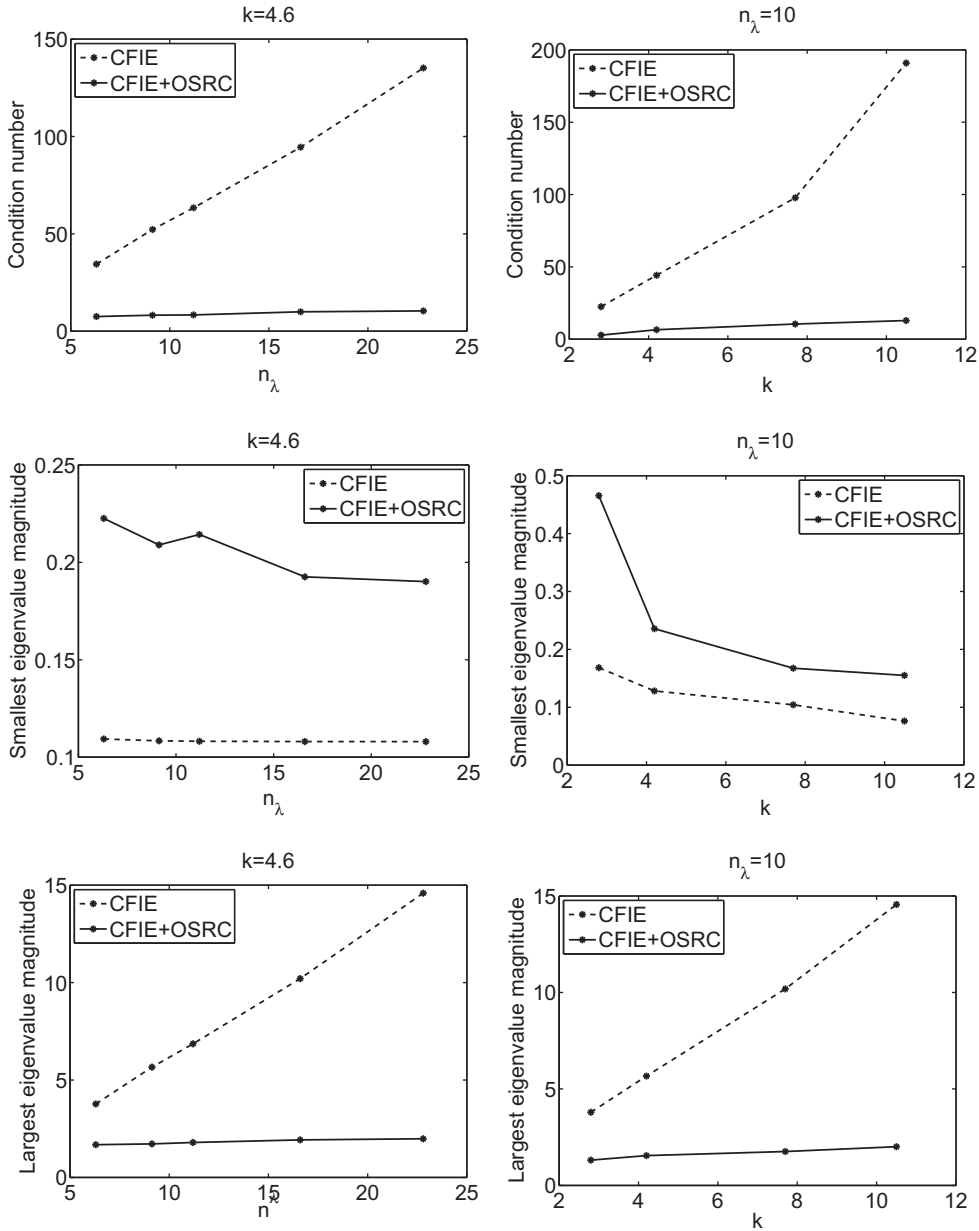


Fig. 15. Cube with cavity: condition number, smallest and largest eigenvalue magnitude – left: versus n_λ , $k = 4.6$; right: versus k , $n_\lambda = 10$.

6.3. Cone-sphere and submarine

The cone-sphere is considered in literature for its sharp apex. We hereby study the eigenvalue behavior for the cone-sphere presented in Section 5. For this example, we consider the Padé order $N_p = 8$. Fig. 20 shows the eigenvalues of the CFIE and the OSRC-preconditioned CFIE operators taking $k = 8.8$ and $n_\lambda = 10$. We report in Fig. 21 the condition number with respect to the wavenumber k for the mesh density $n_\lambda = 10$, and with respect to n_λ for $k = 5.8$. Despite the strong singularity of the geometry, the OSRC-preconditioning technique is again as efficient as for the sphere. In Fig. 21, for the OSRC-preconditioned CFIE, the condition number lies between 1.9 and 2.9 versus n_λ and between 2.1 and 2.15 versus k .

The submarine introduced in Section 5 is considered as a rather realistic example. Let us remind the reader that this object is 43 m long. This explains a choice of smaller wavenumbers. Once more, we consider the Padé order $N_p = 8$. Fig. 22 shows the eigenvalues of the CFIE and the OSRC-preconditioned CFIE operators taking $k = 2.5$ and $n_\lambda = 10$. Fig. 23 gives the condition number with respect to the wavenumber k for the mesh density $n_\lambda = 10$, and with respect to n_λ for $k = 1.5$.

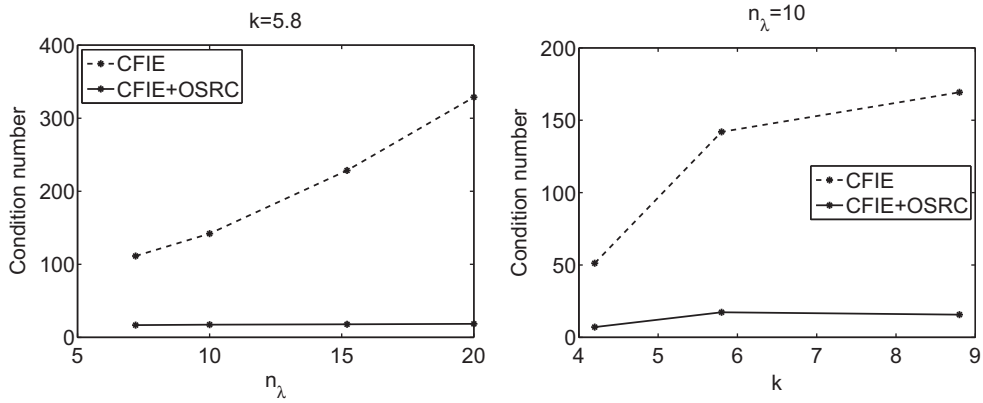


Fig. 16. Sphere with cavity: condition number – left: versus n_λ , $k = 5.8$; right: versus k , $n_\lambda = 10$.

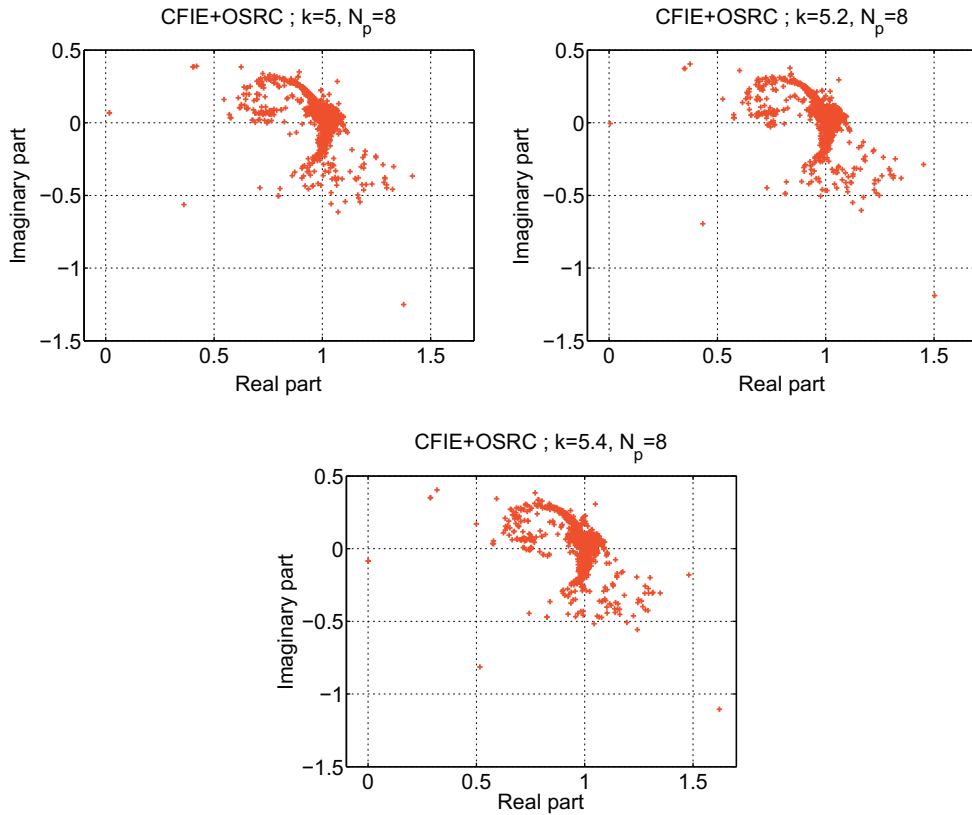


Fig. 17. Cube with cavity: resonance case, around $k = 5.2$.

For the OSRC-preconditioned CFIE, this value lies between 2.5 and 2.9 versus n_λ and between 2.3 and 2.6 versus k . This behavior is also very interesting in view of an iterative solution and even remarkable for the considered object.

7. Numerical results

This section is devoted to numerical simulations validating the OSRC-preconditioned CFIE coupled with the single-level FMM (SLFMM). First, we validate the numerical results with the Mie series solution of the bistatic Radar Cross Section (RCS) of the conducting unit sphere. The RCS is given by

$$\text{RCS}(\theta) = 10 \log_{10}(4\pi |a_0(\theta)|^2), \quad (15)$$

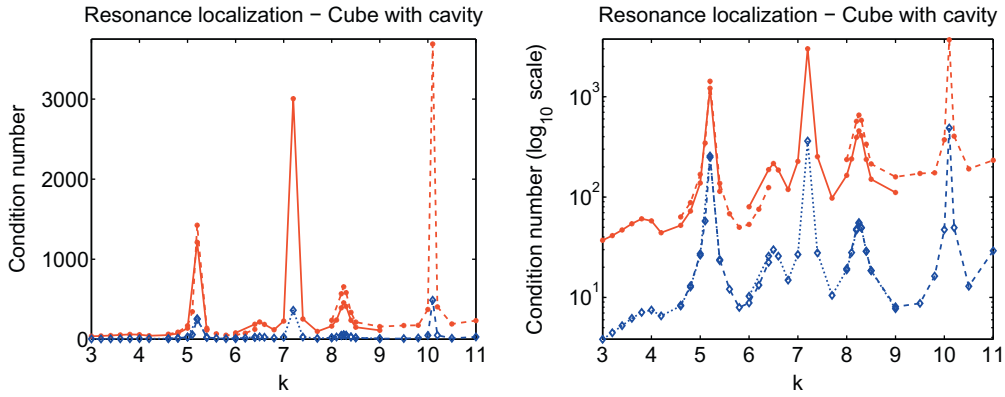


Fig. 18. Cube with cavity: condition number versus wavenumber; left: linear scale, right: log scale.

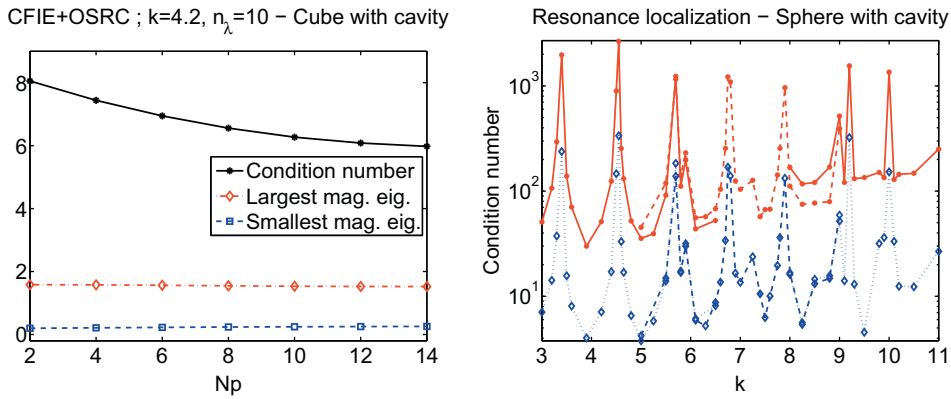


Fig. 19. Left: condition number versus Padé order for the cube with cavity; right: condition number versus wavenumber (log scale) for the sphere with cavity.

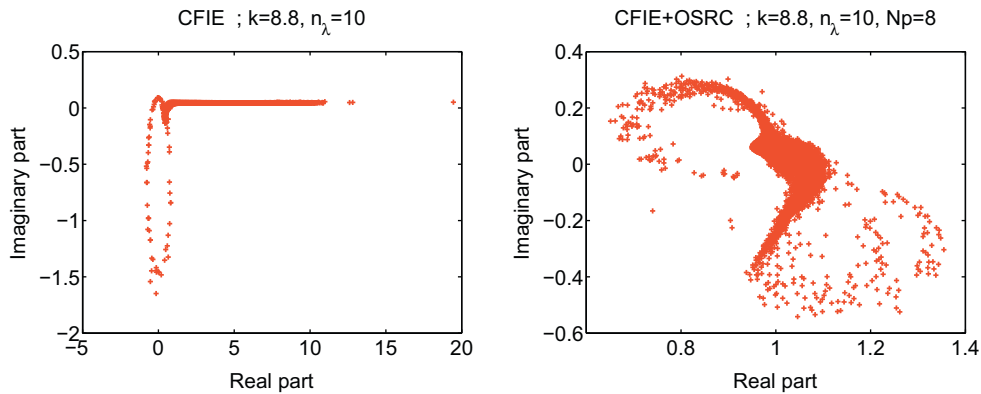


Fig. 20. Cone-sphere: distribution of the eigenvalues, $k = 8.8$, $n_\lambda = 10$.

where θ is the angle of diffusion and $a_0(\theta)$ the scattering amplitude. Then, we test the method on the different scatterers considered in previous sections. These non-smooth objects are not in the functional setting considered in this paper for the well-posedness of the usual and OSRC-preconditioned CFIEs. However, the usual CFIE has been solved successfully for many industrial test-cases in this context. For all scatterers, we examine the influence of an increase of the frequency and of a mesh density on the GMRES convergence. The convergence criterion for all the presented examples is identical: the iterations are stopped when the initial residual has decreased by a factor of 10^{-3} . As expected, all numerical experiments attest

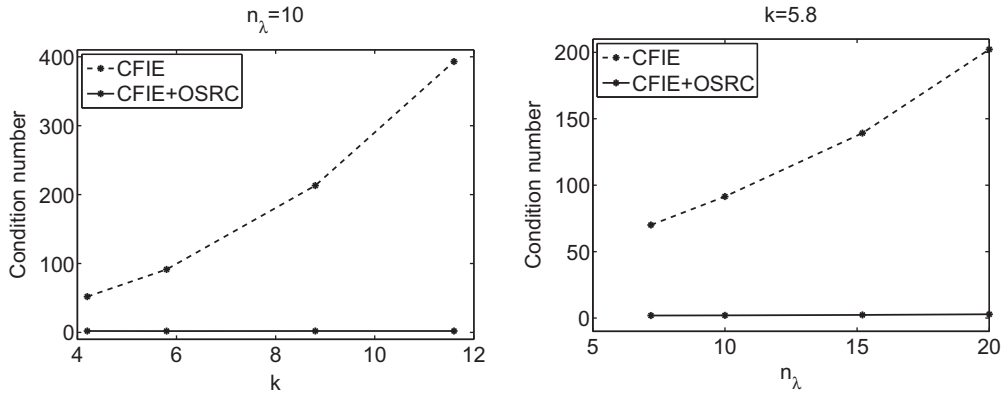


Fig. 21. Cone-sphere: condition number – left: versus k , $n_\lambda = 10$; right: versus n_λ , $k = 5.8$.

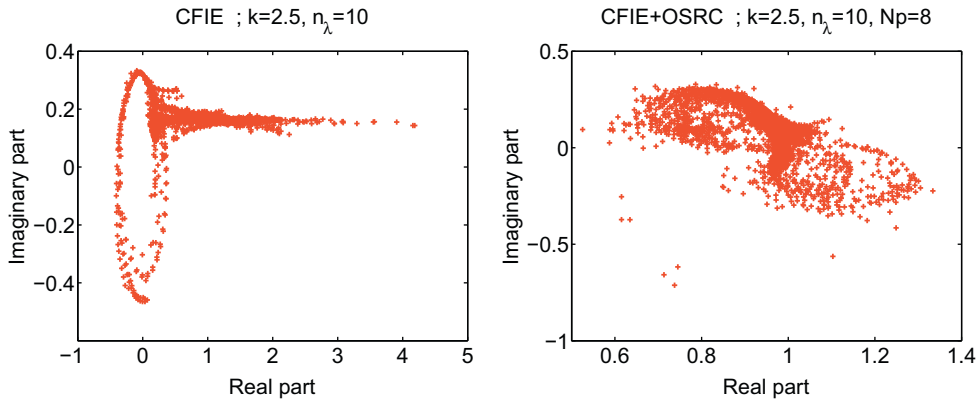


Fig. 22. Submarine: distribution of the eigenvalues, $k = 2.5$, $n_\lambda = 10$.

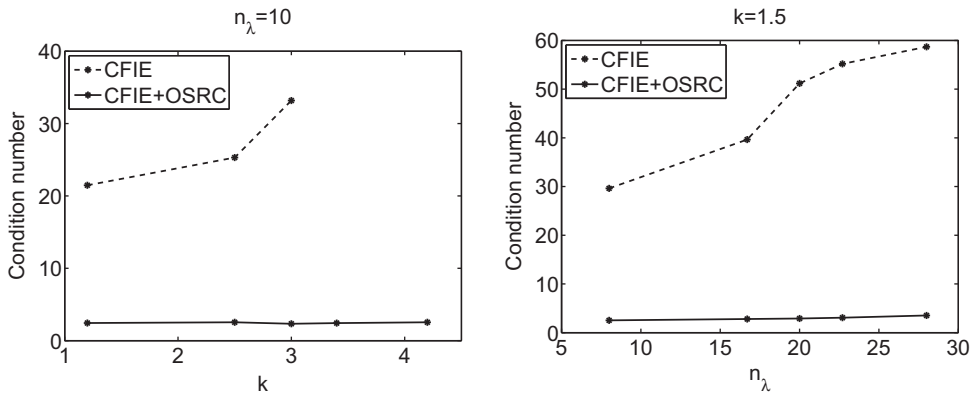


Fig. 23. Submarine: condition number – left: versus k , $n_\lambda = 10$; right: versus n_λ , $k = 1.5$.

the spectral analysis described previously. The considered meshes were obtained using Gmsh [32]. All the tests were run on an Intel (R) Xeon (R) CPU – E5620 – 2.40 GHz.

7.1. Unit sphere

As a usual validation test, we first consider the unit sphere. For all the presented results in this section, the incident wave is a plane wave with incident direction $-\xi^{\text{inc}} = (0, 0, -1)$. Concerning the complex Padé approximation, we fix $N_p = 2$. Fig. 24

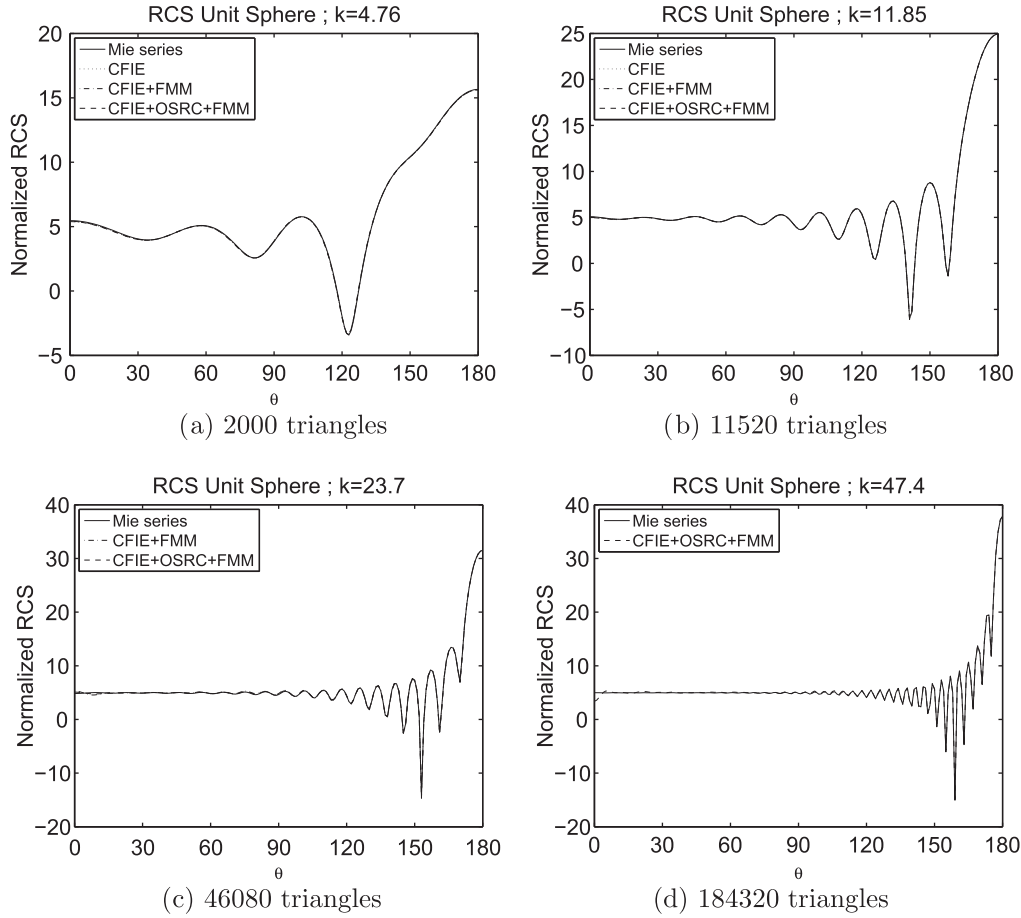


Fig. 24. Normalized RCS for various wavenumbers k ($n_z = 10$).

Table 1

Relative $\|\cdot\|_2$ and $\|\cdot\|_\infty$ errors on the normalized RCS ($n_z = 10$).

k	CFIE		CFIE + FMM		CFIE + OSRC + FMM	
	$\ \cdot\ _2$	$\ \cdot\ _\infty$	$\ \cdot\ _2$	$\ \cdot\ _\infty$	$\ \cdot\ _2$	$\ \cdot\ _\infty$
4.76	6.3e-3	7.9e-3	5.5e-3	6.7e-3	6.8e-3	8.2e-3
11.85	2.5e-3	2.9e-3	3.9e-3	4.9e-3	2.2e-3	2.3e-3
23.7	–	–	1.67e-2	2.07e-2	1.02e-2	9.3e-3
47.4	–	–	–	–	2.46e-2	4.21e-2

shows the RCS for different wavenumbers from $k = 11.85$ to $k = 47.4$ taking $n_z = 10$. One can check that the results obtained with our approach match with the Mie Series solution. The relative errors are given in Table 1. The OSRC-preconditioned CFIE formulation yields the same accuracy as the CFIE.

To validate the efficiency of the preconditioner, we now focus on the GMRES convergence versus the mesh density for a given wavenumber or versus the wavenumber for a given mesh density. We plot in Fig. 25 the number of iterations to reach convergence with respect to k for $n_z = 10$ (left) and with respect to n_z for $k = 10$ (right). The number of iterations drastically increases with both wavenumber and density of discretization per wavelength for the codes without OSRC preconditioning (CFIE or CFIE + FMM). On the contrary, we can see that it is independent of these two parameters when we use the OSRC preconditioning technique. These numerical 3-D high-frequency tests well fit with the previous eigenvalue analysis.

More precisely, in Table 2, we show the CPU costs of the different codes (with or without SLFMM; with or without OSRC preconditioning). More details are given in Tables 3 and 4. In these tables, we use the following notations.

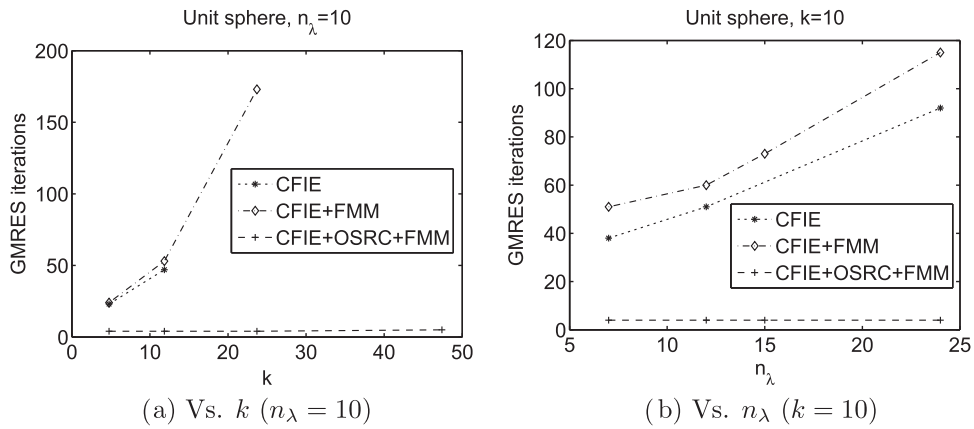


Fig. 25. Unit sphere: convergence of GMRES solver.

Table 2
Global costs versus k taking $n_\lambda = 10$.

k	Total CPU time CFIE	Total CPU time CFIE + SLFMM	Total CPU time CFIE + SLFMM + OSRC
4.76	7 min 42"	13 min 47"	2 min 42"
11.85	9 h 43 min	4 h 33 min	32 min 40"
23.7	> 15 days	214 h 44 min	6 h 20 min
47.4	–	–	48 h 48 min

Table 3
Precomputation and global resolution cost versus k taking $n_\lambda = 10$.

Case	k	T00	T0F	T0P	Tg	Nit
C	4.76	7 min 40"	–	–	2"56	23
CF	4.76	–	8"34	–	13 min 13"	25
COF	4.76	–	8"34	3.6×10^{-2}	2 min 33"	4
C	11.85	9 h 39 min	–	–	3 min 49"	47
CF	11.85	–	8 min 24"	–	4 h 24 min	53
COF	11.85	–	8 min 24"	3.5×10^{-2}	24 min 15"	4
CF	23.7	–	10 min 42"	–	214 h 33 min	173
COF	23.7	–	10 min 39"	1"63	6 h 09 min	4
CF	47.4	–	–	–	–	–
COF	47.4	–	18 h 22 min	8"35	30 h 25 min	5

Table 4
Computation costs per GMRES iteration versus k taking $n_\lambda = 10$.

Case	k	Tit	Tmv	Tc	Tf	To
C	4.76	1.1×10^{-1}	1.1×10^{-1}	–	–	–
CF	4.76	31"74	–	29"14	2"6	–
COF	4.76	38"34	–	35"24	3"09	1.8×10^{-2}
C	11.85	4"88	4"88	–	–	–
CF	11.85	4 min 59"	–	4 min 15"	43"84	–
COF	11.85	6 min 03"	–	5 min 08"	54"73	6.4×10^{-2}
CF	23.7	1 h 14 min	–	1 h 13 min	1 min 08"	–
COF	23.7	1 h 32 min	–	1 h 31 min	1 min 23"	2.5×10^{-1}
CF	47.4	–	–	–	–	–
COF	47.4	6 h 05 min	–	5 h 45 min	20 min 13"	1"12

- CPU time
 - (T00, T0F, T0P) = precomputation (matrices $[M]$ and $[D]$, close interactions of FMM, OSRC preconditioner)
 - Tg, Tit = Total CPU for the solution of the system, total CPU time per iteration
 - Tmv = Total CPU time for the computation of dense matrix–vector products per iteration
 - Tc (resp. Tf) = Total CPU for the calculation of the close (resp. far) interactions per iteration
 - To = Total CPU for the application of the OSRC preconditioner per iteration
- Nit = Number of iterations to reach convergence of the GMRES solver
- C = CFIE; CF = CFIE + SLFMM; COF = CFIE + SLFMM + OSRC

As one can see, the application of the OSRC preconditioning technique considerably reduces the global cost of the resolution and does not really affect the cost per iteration. Recall that the operators involved in the preconditioning technique are differential operators. Then, the cost of applying the regularizing operator \tilde{V} per iteration is negligible. Thus, the cost per iteration is essentially the one of FMM matrix–vector products. For instance, the global cost is multiplied by 8 when the wavenumber is multiplied by 2 from 23.7 to 47.4. This is precisely the cost of the single-level FMM (SLFMM) since its theoretical complexity is about $(k^2)^{3/2} = k^3$ and $8 = 2^3$.

Remark 1. The use of the FMM should be discussed in this approach. Of course, we would not have been able to run some of the tests without FMM due to the sizes of the discretized systems, but how does the FMM impacts on the OSRC technique? The different tests performed show that the FMM does not affect the OSRC technique as far as the accuracy of the FMM is reasonable. When the mesh density becomes too large, the problem meets with low-frequency regimes. This is clearly visible in Fig. 26 and Table 5 for the case $n_\lambda = 32$ where the code has converged to a wrong solution.

Remark 2. Finally, we conclude this section on the influence of the Padé order on the convergence. For the test-case $k = 47.4$ and $n_\lambda = 10$, we note that only 3 GMRES iterations are required with $N_p = 10$ against 4 taking $N_p = 4, 6, 8$ and 5 for $N_p = 2$. This corroborates the behavior of the condition number for such a scatterer (cf. Fig. 9(a)). The extra cost per iteration added by an increase of the Padé order is negligible (a few seconds). At high-frequencies, the global cost per iteration is about some hours (for instance 6h for $k = 47.4$, essentially due to the FMM cost). So, it is interesting to increase the Padé order and save one iteration or more.

7.2. Cavity domains

We consider first the cube with cavity defined in Section 6.2, hit by an incident plane wave which generates reflexions in the cavity and given by the incident direction $-\xi^{\text{inc}} = -(\sqrt{3}/2, 0, 1/2)$. We consider $N_p = 8$ in agreement with the spectral observations in Section 6. The cost related to the OSRC operator is still negligible compared to the cost related to the integral

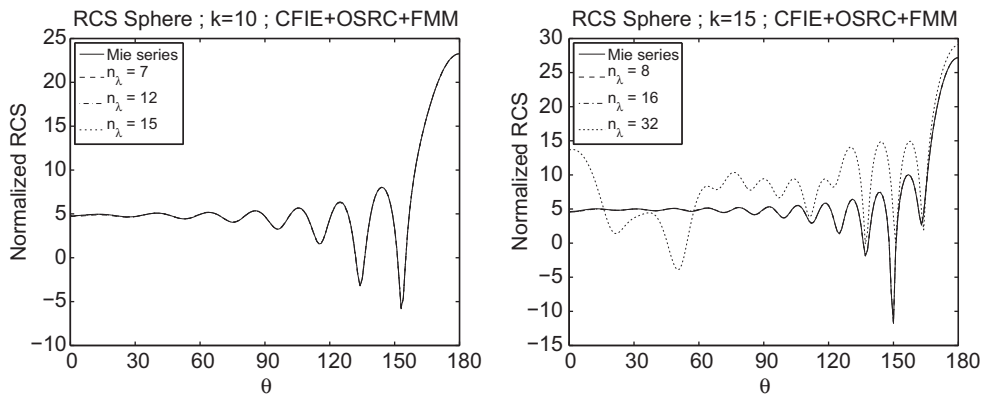


Fig. 26. Normalized RCS for various discretization densities n_λ .

Table 5

Relative $\|\cdot\|_2$ and $\|\cdot\|_\infty$ errors on the normalized RCS ($k = 15$).

n_λ	CFIE		CFIE + FMM		CFIE + OSRC + FMM	
	$\ \cdot\ _2$	$\ \cdot\ _\infty$	$\ \cdot\ _2$	$\ \cdot\ _\infty$	$\ \cdot\ _2$	$\ \cdot\ _\infty$
8	4.1e−3	8.8e−3	7.3e−3	1.1e−2	5.4e−3	4.9e−3
16	2.5e−3	3.4e−3	6.9e−3	1.3e−2	5.3e−3	8.5e−3
32	–	–	–	–	5.3e−1	5.6e−1

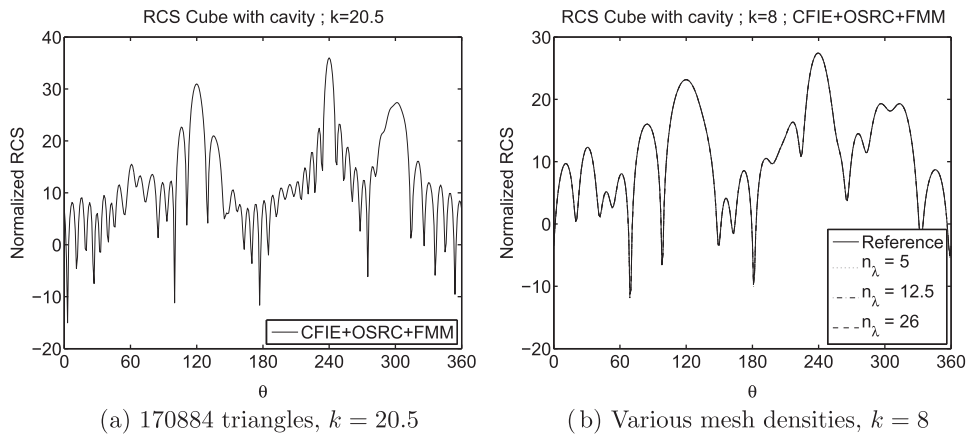


Fig. 27. Normalized RCS.

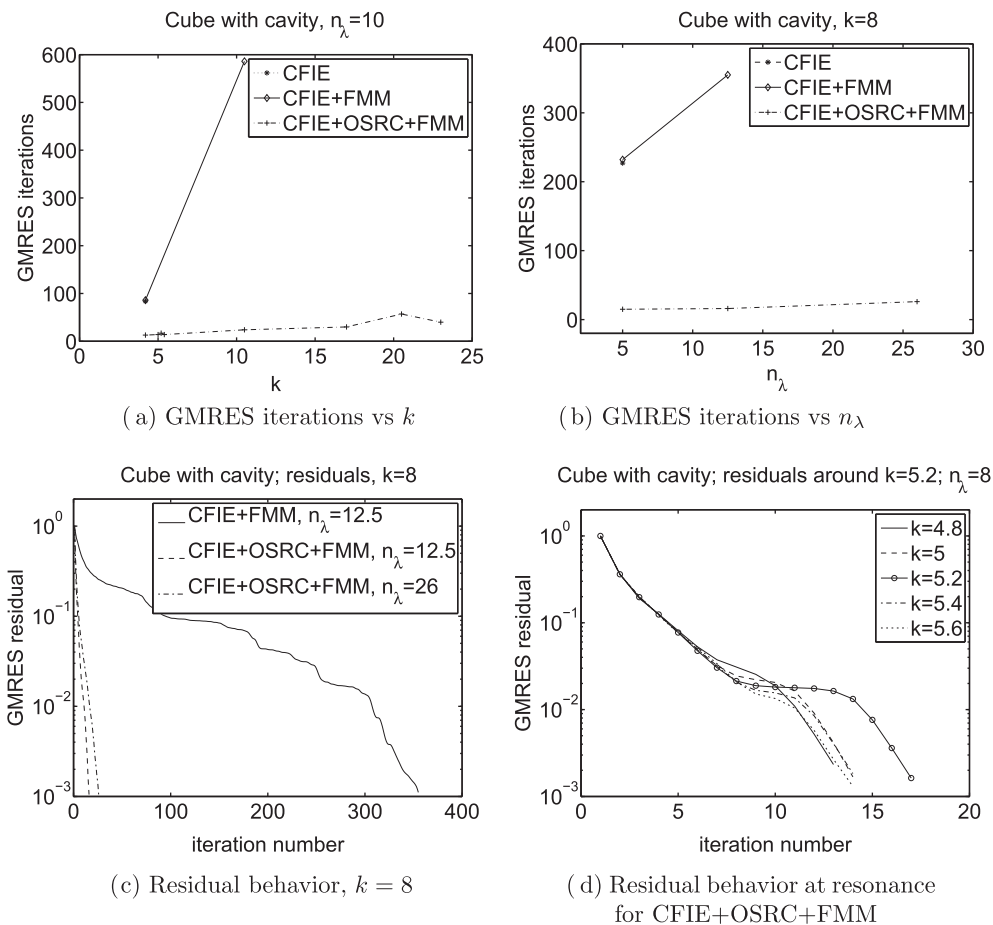


Fig. 28. Convergence of GMRES: iterations and residuals.

operators. Fig. 27 shows the RCS obtained with the code CFIE + OSRC + FMM for different wavenumbers when the mesh density is given by $n_\lambda = 10$ on left, and the same quantity for different mesh densities when the wavenumber is $k = 8$ on right. For the figure on the right, the reference solution is obtained with the code CFIE + FMM with the mesh density $n_\lambda = 12.5$ which is in the usual framework of the FMM. GMRES residuals and the number of GMRES iterations versus wavenumber for the mesh density $n_\lambda = 10$ and versus mesh density for the wavenumber $k = 8$ can be observed in Fig. 28. The number

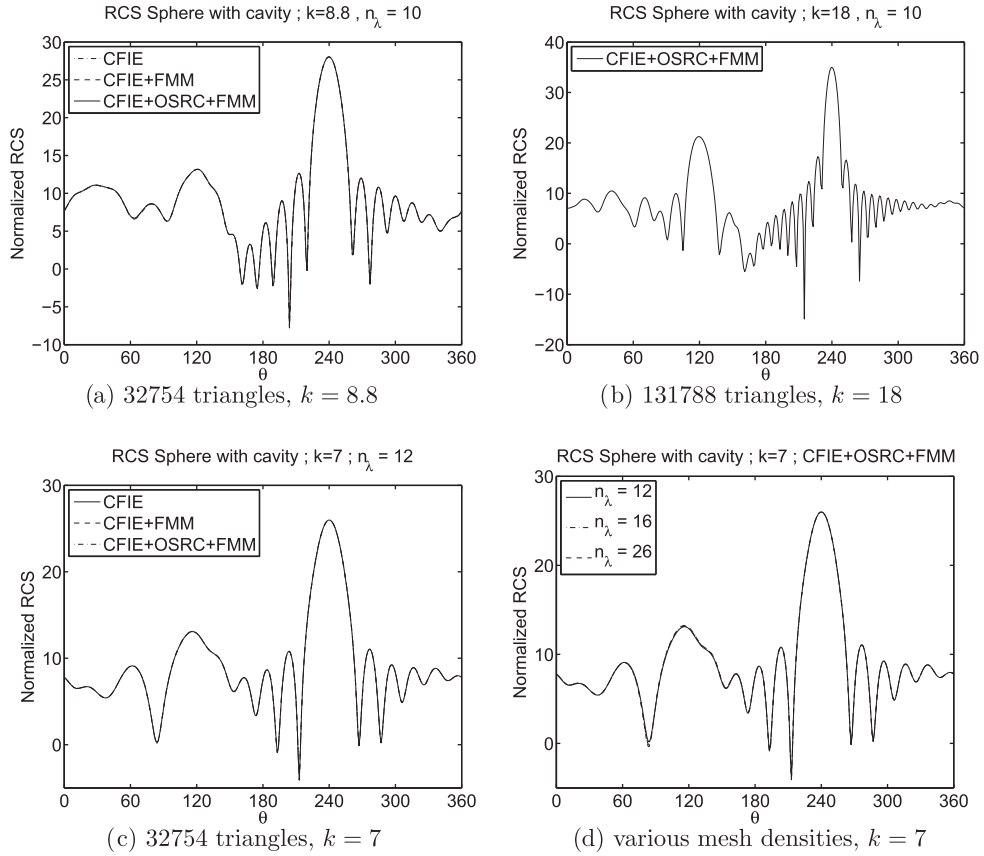


Fig. 29. Normalized RCS.

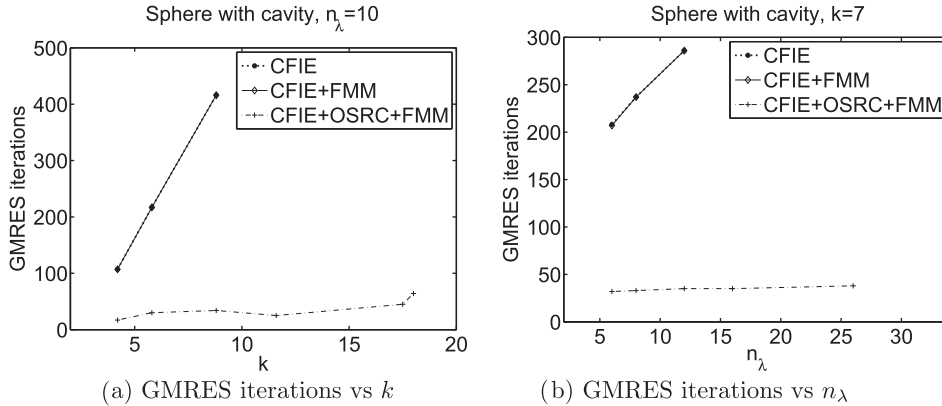
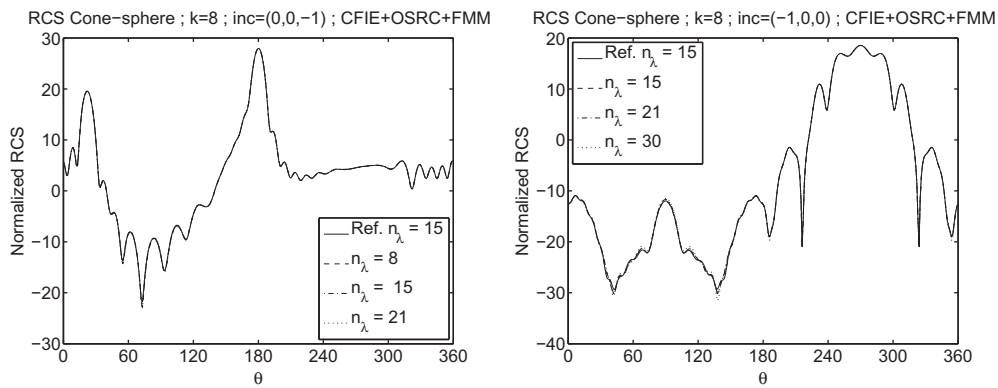
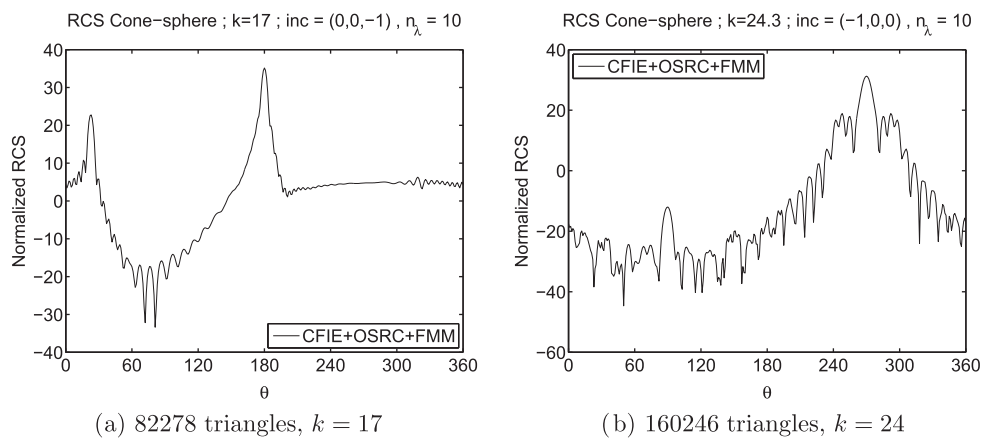


Fig. 30. Convergence of GMRES: iterations and residuals.

of GMRES iterations exactly exhibits the same behavior according to both the parameters k and n_i than the condition numbers of the CFIE operators (cf. Section 6.2). A light peak is visible at the resonant frequency $k = 20$ for the resolution of the OSRC-preconditioned CFIE (the iterative resolution of the CFIE is out of reach at such a frequency). The efficiency of the OSRC-preconditioned CFIE is here again highlighted. Fig. 28(d) shows the residual behavior around a resonance frequency. Close to such a frequency, the presence of small eigenvalues, distributed away from the cluster of eigenvalues at $(1,0)$, slows down convergence of the GMRES. For $k = 5.2$, we can observe a plateau from iteration 7 to 12 in the GMRES residual curve. This plateau is not present in non-resonant cases.

Table 6Number of iterations versus incident direction taking $n_\lambda = 8$, and $k = 8$.

Incident direction	CFIE	CFIE + SLFMM	CFIE + SLFMM + OSRC
(-1,0,0)	171	176	7
(1,0,0)	177	182	7
(0,0,-1)	230	235	7

**Fig. 31.** Normalized RCS for various mesh densities, $k = 8$.**Fig. 32.** Normalized RCS for $n_\lambda = 10$.

Remark 3. In Section 7.1, we mentioned the instability of the FMM. One could overcome the problem of low-frequency regimes by considering larger FMM boxes but this implies an increase of the cost related to the close interactions. Indeed, for the case $k = 8$ and $n_\lambda = 26$, we first considered the automatically suggested level of FMM boxes (level 5) and obtained the convergence indicated in Fig. 28 (26 iterations) and the RCS shown in Fig. 27 (right). Then, we tried the same test case with a lower level (level 4 with larger FMM boxes): The convergence was the same (26 iterations) and the RCS looked very similar but the global CPU cost was multiplied by a factor 2 due to a strong increase of the close interactions. We also considered the same test case with FMM level 5 and OSRC Padé order $N_p = 4$ instead of 8, and obtained convergence after 31 iterations instead of 26. This observation may suggest that the instability of the FMM did not affect the convergence of the code CFIE + OSRC + FMM for mesh densities up to $n_\lambda = 26$, but the choice of the Padé order has to be chosen larger for finer mesh densities in the case of the cube with cavity as suggested by the spectral analysis.

The second trapping domain we consider is the sphere with cavity (Fig. 4) hit by the incident plane wave given by the incident direction $-\xi^{\text{inc}} = -(\sqrt{3}/2, 0, 1/2)$. Some RCS are illustrated in Fig. 29. For example, the RCS obtained for $k = 7$ for various mesh densities (Fig. 29(c)) are in agreement with the reference solutions (Fig. 29(d)): the two plots share the RCS for $n_\lambda = 12$ with the code CFIE + OSRC + FMM. The behavior of the GMRES solver versus the parameters k and n_λ is given in Fig. 30. The results are comparable to what we observe for the cube with cavity.

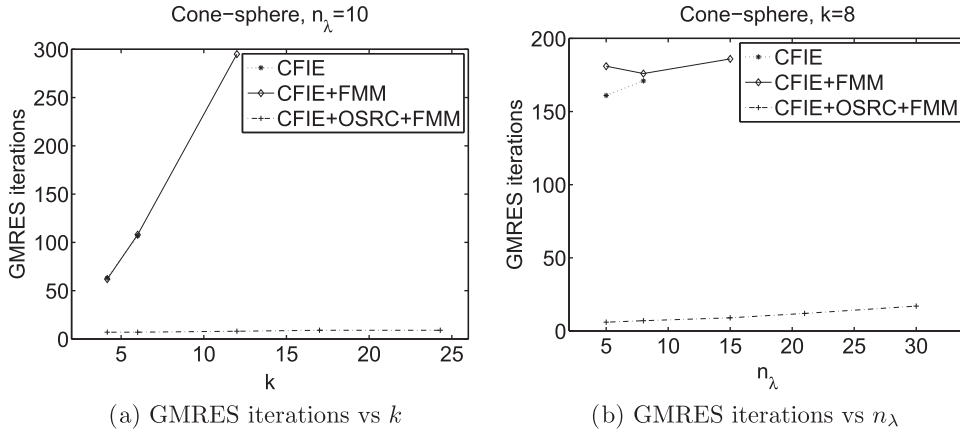


Fig. 33. Convergence of GMRES: iterations and residuals.

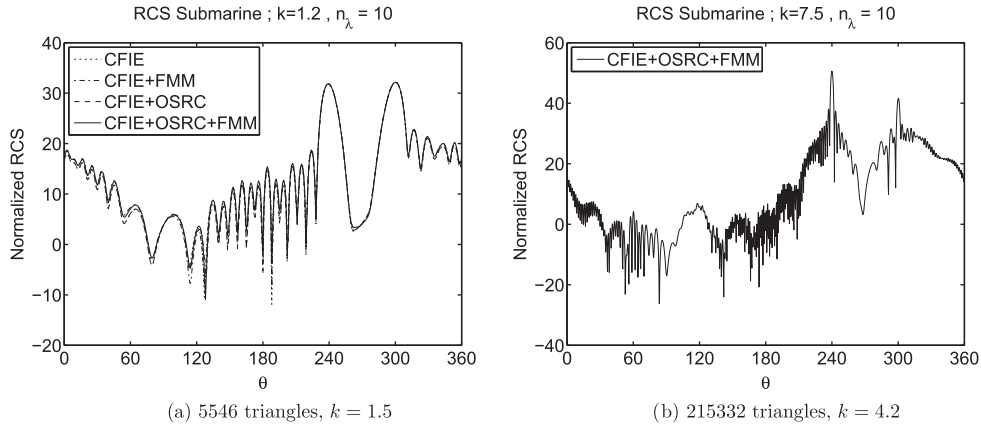


Fig. 34. Normalized RCS: various wavenumbers, $n_\lambda = 10$.

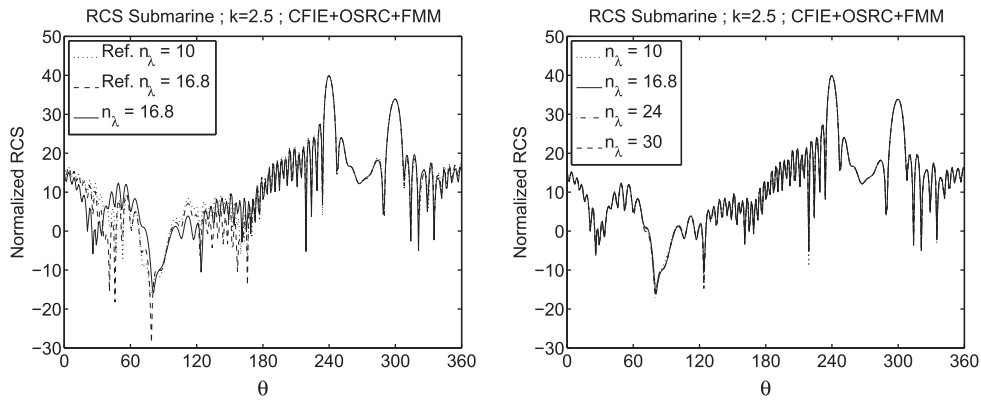


Fig. 35. Normalized RCS: various mesh densities, $k = 2.5$.

7.3. Cone-sphere and submarine – two industrial oriented test-cases

The essential characteristic of the cone-sphere is its sharp apex toward the direction $(1,0,0)$ from its centroid. We then consider three incident directions: $(-1,0,0)$ parallel to the axis of the cone, where the incident wave hits the cone-sphere on the sharp apex, $(1,0,0)$ which hits the sphere part of the cone-sphere, and $(0,0,-1)$ which hits the object perpendicularly to

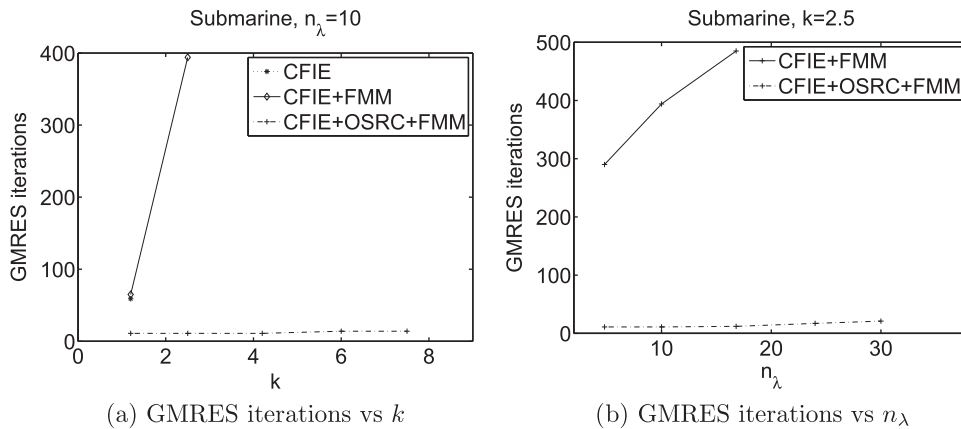


Fig. 36. Convergence of GMRES: iterations and residuals.

its axis. Table 6 indicates how the resolution convergence depends on the incident direction with the code CFIE or CFIE + FMM while it is not the case for the code CFIE + OSRC + FMM. Figs. 31 and 32 give the RCS for different incident directions, wavenumbers or mesh densities. The dependency to the parameters k and n_λ are illustrated in Fig. 33. Let us note again the benefit of the analytical preconditioner.

The case of the submarine is illustrated in Figs. 34, 35 for the RCS and Fig. 36 for the GMRES convergence when the incident direction is $-(\sqrt{3}/2, 0, 1/2)$. For $k = 2.5$, Fig. 35 (right) exhibits the stability of the RCS versus the mesh density obtained with the code CFIE + OSRC + FMM while Fig. 35 (left) indicates that the code CFIE + FMM do not offer the same property. We can guess that this instability is related to the very low convergence of the GMRES. In Fig. 35 (left), the results labeled “Ref” were obtained with the code CFIE + FMM for the mesh densities $n_\lambda = 10$ and $n_\lambda = 16.8$ and do not really match (relative $(-I^2, I^\infty)$ differences: (0.1846, 0.4127)). In Fig. 35 (right), the results are obtained with the code CFIE + OSRC + FMM with mesh densities from 10 to 30 and agree to each other (relative $(-I^2, I^\infty)$ -differences: (0.0212, 0.0679) to (0.0280, 0.1051)). A common curve is visible in both left and right plots of Fig. 35: $n_\lambda = 16.8$ in solid-line style. The instability essentially occurs in the illuminated zone which corresponds to the back of the submarine. Concerning the GMRES convergence, Fig. 36 gives a behavior comparable to what we observed for the unit sphere. The method seems suitable even for such an industrial oriented test-case.

8. Conclusion and perspectives

In this paper, we have drawn a detailed numerical study of the classical and the OSRC-preconditioned CFIEs for the iterative solution of the acoustic sound-hard scattering problem. The developed strategy is based on the use of an OSRC preconditioner to accelerate the chosen iterative solver (GMRES), and the use of the Fast Multipole Method (FMM) to reduce the iteration cost.

A thorough study of the eigenvalue behavior was realized in order to illustrate the impact of the OSRC preconditioning technique on the spectrum of the CFIE operator. Moreover, this spectral analysis allows to precisely understand the influence of the different parameters of the technique, and more specifically of the Padé approximation. This work shows that Padé approximants are an adequate tool. It happens that even a rough approximation leads to good preconditioning properties. As a first conclusion, this experiment attests that the preconditioner fulfills the expected improvements.

The resolution scheme (OSRC preconditioning and FMM) was applied to several numerical test-cases: for smooth and non-smooth obstacles (singularities, cavity domains). The convergence of the GMRES, with respect to both physical and mesh parameters, corroborates the spectral analysis. The speed of convergence is strongly improved by the OSRC preconditioning and the application of FMM does not disturb this benefit. Consequently, only a few GMRES iterations are required to obtain the same accuracy as the CFIE with no preconditioning when we increase the frequency or the mesh density. Moreover, the computation cost follows the FMM behavior: indeed, the algorithm complexity is essentially governed by the FMM due to the low computation cost of the preconditioner. Combining the OSRC preconditioner and the FMM is a very efficient approach to solve the CFIE at high frequencies, even for trapping domains.

However, in the case of trapping domains, near the resonance frequencies, the solver is still slightly influenced by few eigenvalues close to zero. To deal with this issue, the deflated GMRES [42,46] may be a response to avoid this remaining dependance of the convergence for trapping scatterers at resonance frequencies.

The combination presented here can be extended to the iterative resolution of the Maxwell exterior problem using the strategy developed in [25–27]. The OSRC preconditioning approach has already been successfully applied to the impedance case [44]. In a future work, we aim to carry out the study of the spectral behavior of the CFIE and OSRC-preconditioned CFIE

operators for Maxwell exterior problem with perfectly conducting condition, and the study of the contribution of the FMM on the resolution phase.

Acknowledgments

We would like to express our gratitude to Martin Costabel, Professor at the University of Rennes 1, for his helpful expertise on theoretical results, and to Bertrand Thierry, postdoc at the University of Liège, for his participation to the generation of some of the meshes used in the paper.

References

- [1] F. Alouges, S. Borel, D. Levadoux, A stable well-conditioned integral equation for electromagnetism scattering, *J. Comput. Appl. Math.* 204 (2) (2007) 440–451.
- [2] S. Amini, On the choice of the coupling parameter in boundary integral formulations of the exterior acoustic problem, *Appl. Anal.* 35 (1–4) (1990) 75–92.
- [3] S. Amini, S.M. Kirkup, Solution of Helmholtz equation in exterior domain by elementary boundary integral equations, *J. Comput. Phys.* 118 (1995) 208–221.
- [4] X. Antoine, Advances in the on-surface radiation condition method: theory, numerics and applications, in: F. Magoulès (Ed.), *Computational Methods for Acoustics Problems*, Saxe-Coburg Publications, 2008, ISBN 978-1-874672-30-2, pp. 169–194.
- [5] X. Antoine, H. Barucq, A. Bendali, Bayliss–Turkel-like radiation condition on surfaces of arbitrary shape, *J. Math. Anal. Appl.* 229 (1999) 184–211.
- [6] X. Antoine, M. Darbas, Alternative integral equations for the iterative solution of acoustic scattering problems, *Q. J. Mech. Appl. Math.* 58 (1) (2005) 107–128.
- [7] X. Antoine, M. Darbas, Generalized combined field integral equations for the iterative solution of the Helmholtz equation in three dimensions, *M2AN* 41 (1) (2007) 147–167.
- [8] X. Antoine, M. Darbas, Y.Y. Lu, An improved surface radiation condition for high-frequency acoustics scattering problems, *Comput. Meth. Appl. Mech. Eng.* 195 (33–36) (2006) 4060–4074.
- [9] X. Antoine, M. Darbas, *Integral Equations and Iterative Schemes for Acoustic Scattering Problems*, in press.
- [10] T. Betcke, S.N. Chandler-Wilde, I.G. Graham, S. Langdon, M. Lindner, Condition number estimates for combined potential integral operators in acoustics and their boundary element discretization, *Numer. Methods Partial Diff Equ.* 27 (1) (2011) 31–69.
- [11] T. Betcke, E.A. Spence, Numerical estimation of coercivity constants for boundary integral operators in acoustic scattering, *SIAM J. Numer. Anal.* 49 (4) (2011) 1572–1601.
- [12] H. Brakhage, P. Werner, Über das Dirichletsche Aussenraumproblem für die Helmholtzsche schwingungsgleichung, *Arch. Math.* 16 (1965) 325–329.
- [13] O.P. Bruno, T. Elling, C. Turc, Regularized integral equations and fast high-order solvers for sound-hard acoustic scattering problems, *Int. J. Numer. Methods Eng.* 91 (10) (2012) 1045–1072.
- [14] A. Buffa, R. Hiptmair, Regularized combined field integral equations, *Numer. Math.* 100 (1) (2005) 1–19.
- [15] A. Burton, G. Miller, The application of integral methods for the numerical solution of boundary value problems, *Proc. R. Soc. Lond. A* 323 (1971) 201–210.
- [16] B. Carpentieri, I.S. Duff, L. Giraud, Sparse pattern selection strategies for robust Frobenius-norm minimization preconditioners in electromagnetics, *Numer. Linear Algebra Appl.* 7 (2000) 667–685.
- [17] B. Carpentieri, I. Duff, L. Giraud, G. Sylvand, Combining fast multipoles techniques and an approximate inverse preconditioner for large electromagnetism calculations, *SIAM J. Sci. Comput.* 27 (3) (2005) 774–792.
- [18] B. Carpentieri, A matrix-free two-grid preconditioner for solving boundary integral equations in electromagnetism, *Computing* 77 (2006) 275–296.
- [19] G. Chen, J. Zhou, *Boundary Element Methods*, Academic Press, New York, 1992.
- [20] W.C. Chew, J.M. Jin, C.-C. Lu, E. Michielssen, J.M. Song, Fast solution methods in electromagnetics, *IEEE Trans. Antennas Propag.* 45 (3) (2007) 533–543.
- [21] M. Costabel, Boundary integral operators on Lipschitz domains: elementary results, *SIAM J. Math. Anal.* 19 (1988) 613–626.
- [22] R. Coifman, V. Rokhlin, S. Wandzura, The fast multipole method for the wave equation: a pedestrian prescription, *IEEE Antennas Propag. Mag.* 35 (3) (1993) 7–12.
- [23] D.L. Colton, R. Kress, *Integral equation methods in scattering theory*, Pure and Applied Mathematics, John Wiley and Sons Inc., 1983.
- [24] D.L. Colton, R. Kress, *Inverse Acoustic and Electromagnetic Scattering Theory*, Springer-Verlag, 1998.
- [25] M. Darbas, Préconditionneurs analytiques de type Calderon pour les formulations intégrales des problèmes de diffraction d'ondes, Ph.D. Thesis, Toulouse, 2004.
- [26] M. Darbas, Generalized CFIE for the iterative solution of 3-D Maxwell equations, *Appl. Math. Lett.* 19 (2006) 834–839.
- [27] M. Darbas, Some second-kind integral equations in electromagnetism, Preprint, Cahiers du Ceremade 2006-15, 2006.
- [28] E. Darve, The fast multipole method: I. Error analysis and asymptotic complexity, *SIAM J. Numer. Anal.* 38 (1) (2000) 98–128.
- [29] E. Darve, The fast multipole method: numerical implementation, *J. Comput. Phys.* 160 (1) (2000) 195–240.
- [30] E. Darve, P. Havé, Efficient fast multipole method for low-frequency scattering, *J. Comput. Phys.* 197 (2004) 341–363.
- [31] M.G. Duffy, Quadrature over a pyramid or cube of integrands with a singularity at a vertex, *SIAM J. Numer. Anal.* 19 (1982) 1260–1262.
- [32] C. Geuzaine, J.-F. Remacle, Gmsh: a three-dimensional finite element mesh generator with built-in pre- and post-processing facilities, *Int. J. Numer. Methods Eng.* 79 (11) (2009) 1309–1331.
- [33] R.F. Harrington, J.R. Mautz, H-field, E-field and combined field solution for conducting bodies of revolution, *Arch. Elektron. Übertragungstech (AEÜ)* 32 (4) (1978) 157–164.
- [34] D.S. Jones, An approximate boundary condition in acoustics, *J. Sound Vibr.* 121 (1) (1998) 37–45.
- [35] S. Koc, J.M. Song, W.C. Chew, Error analysis for the numerical evaluation of the diagonal forms of the scalar spherical addition theorem, *IEEE Trans. Antennas Propag.* 45 (3) (1997) 533–543.
- [36] R. Kress, Minimizing the condition number of boundary integral operators in acoustic and electromagnetic scattering, *Q. J. Mech. Appl. Math.* 38 (2) (1985) 323–341.
- [37] R. Kress, W.T. Spassov, On the condition number of boundary integral operators for the exterior Dirichlet problem for the Helmholtz equation, *Numer. Math.* 42 (1) (1983) 77–95.
- [38] G.A. Kriegsmann, A. Taflove, K.R. Umashankar, A new formulation of electromagnetic wave scattering using the on-surface radiation condition method, *IEEE Trans. Antennas Propag.* 35 (1987) 153–161.
- [39] Y.G. Liu, W.C. Chew, A low frequency vector fast multipole algorithm, *Commun. Comput. Phys.* 8 (5) (2010) 1183–1207.
- [40] W. McLean, *Strongly Elliptic Systems and Boundary Integral Equations*, Cambridge University Press, Cambridge, UK, 2000.
- [41] F.A. Milinazzo, C.A. Zala, G.H. Brooke, Rational square-root approximations for parabolic equation algorithms, *J. Acoust. Soc. Am.* 101 (2) (1997) 760–766.
- [42] R.B. Morgan, GMRES with deflated restarting, *SIAM J. Sci. Comput.* 24 (2002) 20–37.
- [43] J.-C. Nédélec, *Acoustic and Electromagnetic Equations*, Applied Mathematical Sciences (144), Springer-Verlag, New York, 2001.

- [44] S. Pernet, A well-conditioned integral equation for iterative solution of scattering problems with a variable Leontovitch boundary condition, *ESAIM: M2AN* 44 (2010) 781–801.
- [45] J. Rahola, Diagonal forms of the translation operators in the fast multipole algorithm for scattering problems, *BIT* 36 (2) (1996) 333–358.
- [46] S. Rollin, W. Fichtner, Improving the accuracy of GMRES with deflated restarting, *SIAM J. Sci. Comput.* 30 (2007) 232–245.
- [47] Y. Saad, *Iterative Methods for Sparse Linear Systems*, PWS Publishing Company, Boston, 1996.
- [48] M.E. Taylor, *Pseudodifferential operators*, Princeton Mathematical Series, vol. 34, Princeton University Press, 1981.